SUPPLEMENTARY INFORMATION

Post-Mesozoic Rapid Increase of Seawater Mg/Ca due to Enhanced Mantle-Seawater Interaction

Marco Ligi[1], Enrico Bonatti[1,2], Marco Cuffaro[3] & Daniele Brunelli[1,4]

[1] *Istituto di Scienze Marine, CNR, Via Gobetti 101, 40129 Bologna, Italy.*

[2] *Lamont Doherty Earth Observatory, Columbia University, Palisades, New York 10964, USA.*

[3] *Istituto di Geologia Ambientale e Geoingegneria, CNR, c/o Dipartimento di Scienze della Terra, Sapienza Università di Roma, P.le A. Moro 5, I-00185 Rome, Italy.*

[4] *Dipartimento di Scienze della Terra, Università di Modena, L.go S. Eufemia 19, 41100 Modena, Italy.*

This PDF file includes:

Supplementary Methods

Text

References

Figures (S1 to S11)

Tables (S1 to S5)

* To whom correspondence should be addressed. E-mail: marco.ligi@bo.ismar.cnr.it

SUPPLEMENTARY METHODS

1. Modeling the global ridge system

We simulated mantle dynamics beneath the global mid-ocean ridge system in order to estimate the extent to which mantle peridotites can react with seawater in the ocean basins. Peridotite-seawater reactions can take place at temperatures below 500°C, and are responsible for a variety of chemical exchanges (e.g. Mg, H_2O, CO_2) between solid earth, hydrosphere and biosphere. We divided the global ridge system in 80 sectors each 2048x1024 km, partially overlapping to avoid edge effects. Plate boundaries were digitized from satellite-derived global gravity maps[1] (release 18.1) in Mercator projection at a scale of 1:1000000 (standard parallel: 0° N), with the exception of Gakkel Ridge that was digitized from the map of ref. 2 in Lambert Conformal Conic projection (standard parallels: 84°N and 86°N). Assuming a plate spreading velocity for each sector by averaging spreading rates and directions obtained by Euler vectors of ref. 3, we calculated passive mantle flow, thermal structure and melt production beneath each ridge segment (Tab. S1) taking advantage of Comput-ER (Computing in Emilia Romagna), a common-distributed computing infrastructure.

Comput-ER is based mainly on commodity farms and includes g-Lite GRID and cloud/WNoDeS services. It has been set up within a multidisciplinary context in order to support high-CPU demanding and data-driven applications. In fact, a GRID environment offers a large number of storage and computing resources, and advanced high level job submission services. The submission of jobs on different resource centers reduces consistently processing time. The key solution is based on the jobs execution as loose parallel applications, splitting the input data in several parts, and using a single part of input for the elaboration on each node of the GRID. Once all the input data have been processed, it is possible to merge the global output summing up the results of each elaboration. To exploit this possibility we used the parametric job submission feature of the g-Lite WMS in

order to maximize the resource usage and to optimize the management of the computational tasks.

Sub-lithospheric mantle flow and mantle thermal structure were obtained from the solution of Stokes and heat equations by semi-analytical-pseudo-spectral[4] and finite difference techniques[5], respectively. Depth of isotherms and melt production below a generic ridge-transform-ridge domain are related to (a) spreading rate; (b) length of transform offset and of spreading segments; (c) potential temperature; (d) mantle composition and (e) rheology. The entire sequence of computing programs, requiring as input spreading velocity, plate boundary geometry, mantle potential temperature at the base of the model and mantle source composition, runs on a single computing node (2 Gb RAM, standard OS software) in 24-48 hours and produces 750 Mb of output data. The GRID infrastructure allows the exploration of a wide range of input parameters. Thus, we used a script to submit in a single instance *n*-jobs (one for each mid-ocean ridge sector), achieving *n* solutions within approximately the time of one single run.

1.1 Mantle flow and velocity field

Fluid-mechanical calculations on mantle flow and melting at spreading centers, lead to models either where mantle upwelling and melting are caused solely by plate separation at ridge axis (passive model), or where a dynamic component of mantle flow is required, driven by thermal and compositional buoyancy. In passive flow models the mantle flow pattern is shaped dominantly by viscous drag from rigid plates moving apart, with melt generated in a broad upwelling region. Mantle flow velocity is affected by plate geometry close to ridge axis, and the upwelling velocity can exceed the half spreading rate when the plate thickens rapidly with distance from ridge axis[5-8]. Dynamic flow models require buoyancy forces and low viscosities in the melting region. In these models mantle upwells close to the spreading axis in a region only a few kilometres wide; upwelling is much faster than the half spreading rate, and melt moves vertically primarily due to its buoyancy[9-11].

Focusing of upwelling as predicted by "dynamic" flow models is not clearly seen, implying that flow is mostly passive and driven by plate motion[6]. Thus, we attempted to estimate the mantle thermal structure beneath the global ridge system, adopting mantle passive flow models (Figs S1 and S2). We considered a steady-state mantle flow induced by motion of the overlying rigid plates in an incompressible, homogeneous, isoviscous mantle. The steady-state three-dimensional passive mantle flow has been solved via the Fourier pseudo-spectral technique outlined in ref. 4. We modelled plate thickening passive flow beneath an accretionary plate boundary geometry in a computational frame 2048x1024 km wide and 150 km deep (1x1 km spaced grid points for each 1 km depth increment). The base of the lithosphere, assumed to correspond to the depth of the 800 °C isotherm, was obtained iteratively solving the steady-state advection-diffusion heat equation, starting from the thin plates solution.

1.2 Melting Model

We carried out numerical experiments to estimate mean degree of melting, mean pressure of melting, and mean composition of the aggregate melt beneath a spreading axis. We modelled melt generation, including the effect of water on the peridotite solidus[12], using a modified parameterization of experimental data developed by ref. 13, adding a pressure-dependent H_2O bulk distribution coefficient[14]. We varied the H_2O content of the upper mantle from 0.005 to 0.025 wt%; mantle mineral assemblages for garnet, spinel, and plagioclase peridotite facies are from ref . 15. REE distribution coefficients and source contents are from ref. 16. We assumed that mineral proportions in the transition zone between 85 and 60 km, vary linearly from pure garnet peridotite to pure spinel peridotite. Moreover, we assumed pure-fractional melting and complete melt extraction, but we neglected both latent heat of fusion by freezing of melt, and hydrothermal cooling.

Given that H_2O is about as incompatible as Ce[17], its concentration in the aggregate liquid is inversely proportional to the mean extent of melting. Thus, the water content of the

basaltic glasses for a given degree of melting (i.e. Na_8) constrains the amount of water contained in the mantle source of mid-ocean ridge basalts. The amount of water and Na_2O contained in the aggregated melt has been estimated by varying mean degree of melting (spreading rate and/or mantle potential temperature) and mantle source water content. We assumed a water content of 0.02 wt%, because it fits best the value inferred from global basaltic glasses data, obtained from our unpublished results and from the Petrological Database of the Ocean Floor (PETDB, http://www.petdb.org/) for different spreading rates away from hot spots.

Assuming the melting model outlined above, a plate-thickening passive mantle flow and a temperature of 0 °C at the surface and a constant mantle temperature at 150 km depth (base of our model), ranging from 1300 °C to 1450 °C, we have calculated that the crustal thickness at different spreading rates measured in mid-ocean ridge segments over the global ridge system can be explained best by a mantle potential temperature of 1350 °C at the base model (Fig. S3). The crustal thickness H_c was calculated at any along-axis locations y_0 of a ridge segment by:

$$H_c(y_0) = \frac{\rho_m \dot{M}(y_0)}{\rho_c U_0} \qquad \text{(S1)}$$

where U_0 is the average sea-floor half-spreading rate of the ridge segment; ρ_m and ρ_c are mantle and crustal densities, and $\dot{M}$ is the total volume of melt production per unit time per unit length of ridge. $\dot{M}$ is computed by integrating the melt production rate $\dot{m}$ at along axis location y_0, over the cross-sectional area R in which melting occurs (i.e., over the region where $\dot{m}$ is positive):

$$\dot{M}(y_0) = \iint_R \dot{m}(x, y_0, z)\,dxdz \qquad \text{(S2).}$$

The melt production rate $\dot{m}$ at any location (x,y,z) beneath the ridge is given by:

$$\dot{m}(x, y, z) = \mathbf{v}(x, y, z) \cdot \nabla F(x, y, z) \qquad \text{(S3)}$$

where **v** are the mantle flow velocities and F is the total amount of melting[12,13]. The mean crustal thickness $\overline{H_c^i}$ of the *i-th* ridge segments is obtained by:

$$\overline{H_c^i} = \frac{\int_0^{L_i} H_c(y_0)\,dy_0}{L_i} \tag{S4}$$

where L_i is the length of the *i-th* ridge segment. The mean global crustal thickness is computed by a weighted average over all the segments of the ridge system:

$$\overline{H_c} = \frac{\sum_{i=1}^{N} \overline{H_c^i} L_i}{\sum_{i=1}^{N} L_i} \tag{S5}$$

where N is the total number of ridge segments.

Figure S3 shows that our predicted crustal thickness values ($\overline{H_c^i}$) are lower than those inferred from seismic refraction experiments[18-22] at slow- ultraslow-spreading ridges, and higher than those inferred at fast ridges. This is probably due to the inclusion of the serpentinized mantle in the inferred crustal thickness derived from seismic experiments at slow spreading ridges given the similarity of seismic velocities between lower crust and serpentinites. The assumption of complete melt extraction in predicting crustal thickness may be not valid at fast spreading ridges.

1.3 Volume of mantle rocks that can interact yearly with seawater at T < 150 °C

The amount of cold fluids brought down into the mantle during circulation below ridges depends on the thermal structure of the ridge, which is strongly influenced by rock permeability and spreading rate[23]. Serpentinization itself may affect rock porosity and permeability, causing large volume changes of mantle rocks and therefore rock fracturing.

In our calculations, the thermal structure beneath a segment of the global ridge system depends only on spreading rate and plate boundary geometry; in fact, we neglected latent heat by freezing of melt and hydrothermal cooling. Release of latent heat of fusion by melt

freezing rises the isotherms within the crust, while hydrothermal circulation deepens the isotherms. Thus, the two processes, both acting in the shallow portion of the subridge oceanic lithosphere, tend to balance each other. Moreover, latent heat of fusion is low at ultraslow spreading ridges, where melt production is scarce or absent and where mantle peridotite/seawater interactions are likely to occur. Since we are interested in determining the depths of the 150 °C isotherm, where Mg-release by MORP-seawater reactions may occur, we have neglected hydrothermal cooling in order to be conservative. The along-axis depth-distribution of the 150 °C isotherm was obtained by averaging depths from 10 km-wide across-axis sections. The integral of differences between isotherm depth and crustal thickness (where they are positive) times the full spreading rate gives us an estimate of the volume of mantle-derived mid-ocean peridotites (MORP) that can interact yearly with seawater at a temperature below 150°C at each ridge segment. Figure S4 shows two examples of predicted isotherm depths and crustal thickness along segments of the equatorial Mid Atlantic Ridge offset by long offset transform faults. Mantle-derived peridotite can interact with seawater, other than close to long offset transform faults, only at slow-ultraslow spreading ridges (Fig. S5 and Tab. 1).

2. Mg-loss during peridotite-seawater reactions

We have attempted to measure Mg loss in real rocks as a result of peridotite-seawater reactions (Fig. 1d). We used a set of mantle-peridotites sampled from the Vema Lithospheric Section that exposes lithosphere generated during a 26 Myr time interval at a single Mid Atlantic Ridge segment[24].

We have considered 29 major element analyses of bulk rock[25] (Tab. S2) obtained by X-ray fluorescence at the Department of Earth Sciences of the University of Pisa (Italy). They all show a significant “Loss on Ignition” (LOI), i.e., 11.5 wt% ±1.3, that approximates their H_2O content. The primary bulk rock major elements composition of 31 samples was reconstructed (Tab. S3) from their primary modal composition and the chemical composition of their primary mineral phases from ref. 26. The rocks are spinel-equilibrated harzburgite to lherzolite. The

secondary mineralogy is dominated by serpentine minerals (lizardite ± magnetite) that can reach up to 95 % of the rock (Tab. S3). Serpentinization is dominantly pseudomorphic, with minor serpentine veining accommodating some volume expansion during serpentinization. Samples with carbonate veins have been discarded. In order to reconstruct the bulk rock primary composition (major elements) the composition of olivine needs to be assessed. However, due to the high degree of serpentinization primary unaltered olivine is preserved only in few samples. Therefore olivine composition has been estimated based on best correlations with coexisting orthopyroxene and clinopyroxene phases.

We have based our estimates on regression of compositional trends in MORP using available reliable data for slow and ultra-slow spreading ridges[16,26-44]. Natural samples show compositional scatter revealing that exposed MORPs are often affected by a number of post-melting processes. Accordingly, we have discarded data from samples with evidence of late magmatic interaction/impregnation, and we focused on compositional variations in "purely" residual rocks. The resulting data base includes of 130 samples analyzed for the 4 primary phases olivine, opx, cpx, and spinel. Regressions have been made for each oxide pair in order to derive the correlation between major oxides in pyroxenes and in olivine. Spinel composition shows no significant correlation with olivine composition, while Si, Mg, and Fe in both opx and cpx show significant global correlations with olivine. Regression results and correlation values are reported in Fig. S6 and table S4.

MgO in olivine has been estimated based on MgO and SiO_2 of opx. FeO in olivine was estimated based on SiO_2 and FeO in opx and SiO_2 in cpx. Olivine silica content was estimated based on SiO_2 and FeO in opx, and SiO_2 in cpx. Existing olivine data from the VLS treated as unknown led to oxide estimates within the 1 sigma error of the measured value. Bulk rock primary compositions have been derived by combining primary modal mineralogy and composition of the primary phases. No volume correction has been applied. Volume to weight modal transformations have a negligible effect on the resulting mode given the expected

density of the analyzed phases (Tab. 3). The specific weight difference of the main phases (olivine, opx, cpx) is too small to significantly affect the overall weight distribution.

Equation (2) of ref. 27 allows to estimate the primary MgO_0 content from the altered composition (on an anhydrous base) when the primary bulk composition is not available. This can be done inferring the MgO/SiO_2 ratio from the terrestrial array, and assuming that nothing else (particularly Al_2O_3 and SiO_2) is removed or added to the rock. We calculated Mg loss for the Vema Lithospheric Section (VLS) samples using eqs 2 and 1 of ref. 27. The results (Fig. S7) show that on average 4.1 wt% MgO is extracted from those rocks, in agreement with values inferred from bulk rock reconstructions.

Figure S7 includes also samples of ref. 27 and shows that no correlation exists between estimated Mg loss and crustal age, although most of the samples are from continuous transverse ridges along transform faults. This implies probably early exposition at the seafloor of mantle-derived ultramafics close to the ridge-transform intersection (RTI), and no significant low-T Mg-loss with age.

3. Variations in crustal production and volume of mantle rocks that can interact with seawater at at T < 150 °C over the past 150 Ma

Global cycles, such as sea-level changes[45-46], the carbon cycle[47], and seawater chemistry[48], are assumed to be partly due to temporal variations of the rates of ocean-floor spreading. Based on areal distribution of present-day seafloor age with time since 180 Ma[49] and some tectonic reconstructions[50] it has been suggested that spreading rate could have remained constant over the past 180 Ma. However, recent maps of present day seafloor ages[51,52] and new plate tectonic reconstruction models[52,53] established a curve of seafloor spreading rate and of oceanic crust production rate over the last 150 Ma[54,55], suggesting a strong reduction of spreading and crustal production rate since the Santonian , i.e., 83.5 Ma (Fig. S8).

We calculated plate tectonic reconstructions relative to a fixed Africa plate, based on plate boundaries and finite Euler vectors from refs. 52 and 53, at the same Chrons of constructed seafloor spreading isochrons of ref. 53. Reconstructed positions of continents and mid-ocean ridges were obtained with the Gplates software (*http://www.gplates.org*), at

Chrons: 5o (10.9 Ma), 6o (20.1 Ma), 13y (33.1Ma), 18o (40.1Ma), 21o (47.9Ma), 25y (55.9Ma), 31y (67.7 Ma), 34y (83.5 Ma), M0 (120.4 Ma), M10 (131.9Ma), M16 (139.6 Ma), M21 (147.7 Ma) and M25 (154.3 Ma) (Fig. S9). Half spreading rate at each ridge segment mid-point was computed for each time interval, from stage poles and rotation angles for the relative motions of plates that share a specific mid-ocean ridge boundary. Stage rotations describe the motions of plate during two characteristic ages and were calculated combining the finite rotations, expressed as rotation matrices, in the Africa-fixed reference frame. The mean global spreading rate $\overline{V_s}$ was calculated by a weighted average over all the segments of the ridge system:

$$\overline{V_s} = \frac{\sum_{i=1}^{N} V_s^i L_i}{\sum_{i=1}^{N} L_i} \qquad \text{(S6)}$$

where V_s^i is the spreading rate of the *i-th* ridge segment (Fig. S8a).

Plate boundary geometries and spreading rates of the reconstructed paleo-oceans were used to estimate variations in crustal production and in volume of mantle rocks that can interact with seawater at T < 150 °C over the past 150 Ma, using the same techniques described in previous sections for the current mid ocean ridge system. Results are shown in figures S8b and table S5.

4. Modeling the oceanic mass balance of Mg and Ca through time

There is strong evidence that the ocean has not been at steady state for Mg concentrations over geological time scales. Several studies have modelled the evolution of seawater composition during Phanerozoic[48,56-60], or have estimated changes from fluid inclusions[61-64]; from pore fluid chemistry[65]; from marine biogenic carbonates[66-68]; from ridge flank hydrothermal carbonate veins[69]; and from Mg, B and S isotope composition[70-73]. While there is disagreement over the causes of seawater compositional changes, there is a general consensus that the Mg concentration in seawater has varied during Phanerozoic; in particular, that Mg/Ca has risen over the past 80 Ma as a consequence of both an increase of seawater Mg concentration and a decrease of Ca concentration. We attempt next to model the effect on Mg

and Ca seawater concentration of (a) variations through time of oceanic crustal production and (b) volume of low-temperature mantle hydration related to changes in spreading rates and accretionary plate boundary geometry. The model calculations are based on the paleo-reconstructions described previously. The inferred secular variations of oceanic crust production rate and of volume of low-temperature mantle hydration curves (Tab. S5) were resampled at 1 Ma step after spline interpolation (Fig. 5 and Fig. S8).

4.1 Mg model

We assume a model where secular variations of seawater Mg-content are controlled by: (1) a constant influx from rivers; (2) variable Mg-release flux from peridotite-seawater reactions; (3) variable Mg-removal flux from high-temperature hydrothermal alteration of the basaltic crust as the result of seafloor spreading rate variations; and (4) a constant Mg residual-outflow including low-temperature off-axis hydrothermal-basaltic crust interactions[74-76], reaction with carbonate to form dolomite[58-59], ion-exchange reactions with clays[59].

Changes in the size of the oceanic Mg reservoir are thus calculated as:

$$\frac{d[Mg]}{dt} = F_{rw}^{Mg} + F_{hyP}^{Mg}(t) - F_{hyB}^{Mg}(t) - F_{res}^{Mg} \qquad \text{(S7)}$$

where: F_{rw}^{Mg} is the constant river influx, assumed of $5.6 \cdot 10^{12}$ mol/yr; $F_{hyP}^{Mg}(t)$ is the influx due to MORP-seawater reactions. We let the MORP-derived Mg flux vary through time following the estimated volume of mantle rocks that can interact yearly with seawater at T < 150 °C (Tab. S5). The estimated recent flux is of $1.15 \cdot 10^{12}$ mol/yr, assuming that 100% of MORPs that can potentially react with seawater at T < 150 °C do actually react and lose 5% wt of their MgO content (i.e., $F_{hyP}^{Mg}(0) = 0.05 \cdot \rho_m \cdot P_m(0)/[MgO_{molar\ mass}]$, where ρ_m = 3300 kg/m^3 is the density of mantle rocks and $P_m(0)$ = $2.7769 \cdot 10^8$ m^3/yr is the current volume rate of MORP that interact with seawater at T<150 °C); F_{res}^{Mg} is a constant unknown Mg-residual outflow; and $F_{hyB}^{Mg}(t)$ is the Mg-removal flux by high-temperature hydrothermal circulation at ridge axis, that varies due to variations in the rate of seafloor production (Tab. S5). The relation between rate of

oceanic crust production and high-temperature hydrothermal flux is likely to be nonlinear, considering the complexity of the physical, chemical, and hydrological processes involved. As a first approximation, we assume that variations through time of Mg removal by the high-temperature hydrothermal depend by seawater Mg content and by an hydrothermal flux that scales linearly with variations in mid ocean ridge crustal rate production:

$$F_{hyB}^{Mg}(t) = H_{hT}(t)[Mg]_{sw}(t) = H_{hT}(0)[1+\alpha\frac{P_c(t)-P_c(0)}{P_c(0)}]([Mg]_{sw}(t)) \quad \text{(S8)}$$

where $[Mg]_{sw}(t)$ is the concentration of Mg in seawater at time t and $H_{hT}(0)$ is the modern mid ocean ridge high-T hydrothermal flux, assumed at $5\cdot10^{13}$ kg/yr. Assumed values of $3\cdot10^{13}$ and $5.2\cdot10^{13}$ kg/yr (range of the estimated high-T hydrothermal flux) do not change main results. $P_c(0)$=$2.0355\cdot10^{10}$ m^3/yr is the current oceanic crustal production rate; $P_c(t)$ is the production rate through time (Tab. S5); and α is a scale factor. Figure S10 shows modeled Mg inflow and outflow fluxes since 150 Ma.

4.2 Ca model

Secular variations of seawater Ca-content have been modelled assuming: a constant river influx F_{rw}^{Ca} of $1.4\cdot10^{13}$ mol/yr; a variable influx $\hat{F}_{hyB}^{Ca}(t)$ due to Ca release during low and high temperature hydrothermal circulation at mid ocean ridges; a variable outflux $F_{wBP}^{Ca}(t)$ related to oceanic seafloor alteration; and an unknown constant residual Ca-outflow F_{res}^{Ca} including: Ca-fixation due to carbonate accumulation (biogenic and inorganic), and anhydrite precipitation. Thus, changes through time of seawater Ca-content can be described by:

$$\frac{d[Ca]}{dt} = F_{rw}^{Ca} + \hat{F}_{hyB}^{Ca}(t) - F_{wBP}^{Ca}(t) - F_{res}^{Ca} \quad \text{(S9)}$$

with

$$F_{wBP}^{Ca}(t) = F_{wMORB}^{Ca}(t) + F_{wMORP}^{Ca}(t) \quad \text{(S10)}$$

where $F^{Ca}_{wMORB}(t)$ and $F^{Ca}_{wMORP}(t)$ are the outflow relate to alteration at seafloor of mid-ocean-ridge basalts (MORB) and of exposed mantle rocks, respectively. Secular variations of the net flux due to Ca-release by hydrothermal circulation and Ca-capture by MORB alteration as a result of variations of oceanic crust production (Tab. S5) can be approximated by:

$$F^{Ca}_{hyB}(t) = \hat{F}^{Ca}_{hyB}(t) - F^{Ca}_{wMORB}(t) = \hat{F}^{Ca}_{hyB}(0)[1 + a\frac{P_c(t) - P_c(0)}{P_c(0)}] - F^{Ca}_{wMORB}(0)[1 + b\frac{P_c(t) - P_c(0)}{P_c(0)}] =$$

$$= F^{Ca}_{hyB}(0)[1 + \beta\frac{P_c(t) - P_c(0)}{P_c(0)}] \qquad (S11)$$

where $\hat{F}^{Ca}_{hyB}(0)$, $F^{Ca}_{wMORB}(0)$, $F^{Ca}_{hyB}(0)$ are the modern mid ocean ridge hydrothermal flux, MORB alteration flux and MORB hydrothermal-weathering net inflow, respectively; and *a*, *b* and β are scale factors. Estimated modern fluxes of Ca caused by hydrothermal Ca-release $\hat{F}^{Ca}_{hyB}(0)$ and Ca-fixation during oceanic seafloor alteration $F^{Ca}_{wBP}(0)$ are <$4.8 \cdot 10^{12}$ and 1.5-$2.4 \cdot 10^{12}$ mol/yr, respectively[57]. During episodes of amagmatic spreading, along slow-spreading ridges detachments and core complexes unroof the mantle through faulting, allowing exposure of peridotites at the seafloor[77]. These processes may occur along a significant portion of the Atlantic (up to 25%) with peridotites making up as much as 75% of the deeper rocks exposed[78-81]. Several stretches of ultra-slow spreading ridges, characterized by amagmatic accretion, expose mantle peridotites, as well as long-offset transform faults. We can estimate that at least 20% of the current seafloor at mid ocean ridges is floored by peridotites. Thus, the total modern Ca-fixation flux due to alteration of the oceanic seafloor (assumed at $2.4 \cdot 10^{12}$ mol/yr) may be attributed to:

$F^{Ca}_{wMORB}(0) = 80\%\ F^{Ca}_{wBP}(0) = 1.9 \cdot 10^{12}$ mol/yr and $F^{Ca}_{wMORP}(0) = 20\%\ F^{Ca}_{wBP}(0) = 0.5 \cdot 10^{12}$ mol/yr.

Ophicalcites occur associated with ocean-continent transitions (W-Iberian margin, Alpine Tethys) or slow-spreading ridges and transform zones. They were never observed in the Semail (Oman) and Troodos ophiolites, believed to represent lithosphere produced at intermediate spreading rate (D. Bernoulli, pers. comm.). In ophicalcites hosted by serpentinites, dolomite is very rare and usually of secondary origin. Cements are typically calcite (probably neo-morphic

after aragonite) or aragonite[82]. This suggests that alteration of mantle rocks exposed at the seafloor can capture some Ca rather than Mg. Ca can be extracted from seawater following serpentinization, as observed for instance at the Lost City site[83].

We assume a modern MORB hydrothermal-weathering net inflow $F_{hyB}^{Ca}(0)$ of $1.25 \cdot 10^{12}$ mol/yr. Assumed values of $0.8 \cdot 10^{12}$ and $1.5 \cdot 10^{12}$ mol/yr (range of the estimated hydrothermal flux) do not change main results. In addition, we assume variations through time of Ca-removal by MORP weathering $F_{wMORP}^{Ca}(t)$ that scales linearly with variations in volume of mantle rocks that can interact yearly with seawater at T < 150 °C (Tab. S5)

$$F_{wMORP}^{Ca}(t) = F_{wMORP}^{Ca}(0)[1 + \gamma \frac{P_m(t) - P_m(0)}{P_m(0)}] \qquad \text{(S12)}$$

where $P_m(0)$ is the current volume rate of MORP that interact with seawater at T<150 °C; $P_m(t)$ is the volume rate through time (Tab. S5); and γ is a scale factor.

Given the above (S9) can be written as:

$$\frac{d[Ca]}{dt} = F_{rw}^{Ca} + F_{hyB}^{Ca}(t) - F_{wMORP}^{Ca}(t) - F_{res}^{Ca} \qquad \text{(S13).}$$

Numerical solutions of eqs. (S7) and (S13) were reached by finite difference approximation (Crank–Nicolson implicit scheme) using an integration time step of 1 Ma and initial (150 Ma) Mg- and Ca-seawater concentrations ([Mg] = 30.5 mmol/kg H_2O and [Ca] = 24 mmol/kg H_2O), inferred from halite fluid inclusions[63]. The unknown residual fluxes F_{res}^{Mg} and F_{res}^{Ca} were solved iteratively to fit the modern Mg- and Ca-seawater concentrations ([Mg] = 53 mmol/kg H_2O and [Ca] = 10.5 mmol/kg H_2O).

Numerical modelling clearly show that Mg-released by low-temperature MORP-seawater reactions contributed to the sharp increase of seawater Mg-concentration around 70-60 Ma. In addition, Mg-output decreased due to a rapid lowering of oceanic crust production since 83.5 Ma (Santonian) (Fig. 1c). Decreasing Ca-release due to a lower hydrothermal flux after the

Santonian decreases seawater Ca-concentration. The Mg/Ca, as a consequence of temporal variations of both Mg and Ca seawater concentrations, stayed close to 1 during the Late Cretaceous and rose up to the current value of ~5.1 during the last 70 Ma, with a rate that increases gradually toward the present day. The maximum rate of Mg/Ca increase recorded at ~20 Ma may account for the rapid change of Mg/Ca during the last 10 Ma inferred from pore fluid chemistry[65].

4.3 Constraints from Mg isotope ratios

The Mg isotope budget of the oceans may provide constraints on the relative contribution of the two major sinks for Mg: hydrothermal circulation in basalt, and dolomite deposition. Following ref. 71, we considered the Mg isotope budget of the oceans through time, including the effect of Mg-released by MORP/seawater reactions, assuming the Mg-fluxes estimated by our model. Considering first the residual Mg-outflow F_{res}^{Mg} of our model, we assume here that it is due only to off-axis low-temperature hydrothermal circulation within basalts F_{hyO}^{Mg} and dolomite accumulation F_{dol}^{Mg}:

$$F_{res}^{Mg} = F_{hyO}^{Mg} + F_{dol}^{Mg} \Rightarrow F_{hyO}^{Mg} = a(t)F_{res}^{Mg};\ F_{dol}^{Mg} = b(t)F_{res}^{Mg} \qquad \text{(S14)}$$

where *a* and *b*, are fractions of the residual flux due to off-axis hydrothermal circulation and dolomite deposition, respectively. $a(t) + b(t) = 1 \ \ \forall t \in \Re^{+}$.

The rate of change through time of seawater $^{26}Mg/^{24}Mg$ in the oceans may be derived from the conservation equations for the individual isotopes:

$$\frac{d\,\delta_{sw}^{^{26}Mg}(t)}{dt} = \left\{ \begin{array}{l} F_{rw}^{Mg}[\delta_{rw}^{^{26}Mg} - \delta_{sw}^{^{26}Mg}(t)] + F_{hyP}^{Mg}(t)[\delta_{hyP}^{^{26}Mg} - \delta_{sw}^{^{26}Mg}(t)] - \\ - F_{hyB}^{Mg}(t)[\delta_{hyB}^{^{26}Mg} - \delta_{sw}^{^{26}Mg}(t)] - \\ - F_{res}^{Mg}\left[a(t)[\delta_{hyO}^{^{26}Mg} - \delta_{sw}^{^{26}Mg}(t)] + b(t)[\delta_{dol}^{^{26}Mg} - \delta_{sw}^{^{26}Mg}(t)]\right] \end{array} \right\} \Big/ N_{Mg}(t) \qquad \text{(S15)}$$

where $\delta_{sw}^{^{26}Mg}$, $\delta_{rw}^{^{26}Mg}$, $\delta_{hyP}^{^{26}Mg}$, $\delta_{hyB}^{^{26}Mg}$, $\delta_{hyO}^{^{26}Mg}$ and $\delta_{dol}^{^{26}Mg}$ are the $\delta^{26}Mg$ of seawater, of river waters, of MORP/seawater reactions related fluids, of high-temperature hydrothermal fluids, of low-

temperature off-axis hydrothermal fluids and of dolomite, respectively. N_{Mg} *is* the total number of moles of Mg in the ocean. We assume that current best estimated values for δ^{26}Mg of rivers (-1.09), for MORP (-0.36) and dolomite (-2.0) did not change through time. We assume also no Mg isotopic fractionation during MORP/seawater reactions. In addition, we assume that no Mg is returned to the ocean from both high- and low-temperature hydrothermal circulation within basalts. This last assumption implies that $\delta_{hyB}^{26Mg} = \delta_{hyO}^{26Mg} = \delta_{sw}^{26Mg}$, and eq. (S13) reduces:

$$\frac{d\,\delta_{sw}^{26Mg}(t)}{dt} = \left\{ \begin{array}{l} F_{rw}^{Mg}\left[\delta_{rw}^{26Mg} - \delta_{sw}^{26Mg}(t)\right] + F_{hyP}^{Mg}(t)\left[\delta_{hyP}^{26Mg} - \delta_{sw}^{26Mg}(t)\right] - \\ - b(t) F_{res}^{Mg}\left[\delta_{dol}^{26Mg} - \delta_{sw}^{26Mg}(t)\right] \end{array} \right\} \Big/ N_{Mg}(t) \qquad \text{(S16).}$$

We explore next three possible scenarios:

(i) The ocean is at steady state with respect to Mg isotopic composition;

(ii) Non steady state scenario for δ^{26}Mg of seawater and constant accumulation of dolomite;

(iii) Non steady state scenario for δ^{26}Mg of seawater as well as for dolomite.

(i) Assuming that no change of seawater δ^{26}Mg occurred through time, eq. (S16) allows to infer variations of dolomite deposition:

$$b(t) = \frac{\left\{F_{rw}^{Mg}\left(\delta_{rw}^{26Mg} - \delta_{sw}^{26Mg}\right) + F_{hyP}^{Mg}(t)\left(\delta_{hyP}^{26Mg} - \delta_{sw}^{26Mg}\right)\right\}}{F_{res}^{Mg}\left(\delta_{dol}^{26Mg} - \delta_{sw}^{26Mg}\right)} \qquad \text{(S17)}$$

where δ_{sw}^{26Mg} =-0.82 (ref. 71).

Figure S11a shows modelled variations of Mg-removal flux due to dolomite deposition since 150 Ma. Dolomite Mg-removal flow ranges from ~22% of the river input (implying F_{hyO}^{Mg} = ~32% of the river input) during the Cretaceuos, to 15 % (implying F_{hyO}^{Mg} = ~39% of the river input) during the Cenozoic (volume fraction of MORP interacting at low-T with seawater = 100%). Note that when the effect of Mg-released by MORP/seawater reactions is added

(volume of MORP interacting at lowT with seawater > 0), modelled fluxes and the percentage of dolomite in carbonate sediments of ref. 84 correlate.

(ii) We let seawater δ^{26}Mg vary through time. If we assume that dolomite deposition has been constant through time, the fraction *b* of F_{res}^{Mg} can be solved iteratively from eq. (S16) by fitting the modern seawater δ^{26}Mg value (-0.82). Dolomite Mg-removal fluxes range from 15.7% of the river input (volume fraction of MORP interacting at low-T with seawater = 100%) to 23% of the river input (volume fraction of MORP interacting at low-T with seawater = 0%), regardless of the initial value of 150 Ma seawater δ^{26}Mg (Fig. S11b).

(iii) We let the δ^{26}Mg of seawater and dolomite deposition vary through time. In this case *b(t)* is undetermined and additional constraints are needed. Several lines of evidence show that dolomite deposition prevailed during the Cretaceous, in contrast with the prevailing carbonate deposition that occurred during the Cenozoic. It has been also suggested that as much as 90% of seawater Mg is lost to a dolomite sink during enhanced periods of dolomitization[56]. Such a large dolomite sink would induce a huge shift in the δ^{26}Mg of seawater toward values heavier (Fig. S11c) than those of modern seawater δ^{26}Mg (-0.82), in contrast with data from echinoderms[85] suggesting that seawater δ^{26}Mg stayed approximately constant and close to the modern value during the last 350 Ma, except for a negative excursion occurring at around 100 Ma. We conclude that the Mg isotopic chemistry is consistent (compatible) with a lowered dolomite deposition and increased MORP-seawater interaction in the Cenozoic and modern oceans.

References

1. Sandwell, D. T. & Smith, W. H. F. Marine gravity anomaly from Geosat and ERS-1 satellite altimetry. *J. Geophys. Res.* **102**, 10039–10054 (1997).
2. Michael, P. J., Langmuir, C. H., Dick, H. J. B., Snow, J. E., Goldstein, S. L., Graham, D. W., Lehnert, K., Kurras, G., Jokat, W., Muhe, R. & Edmonds, H. N. Magmatic and amagmatic seafloor generation at the ultraslow-spreading Gakkel ridge, Arctic Ocean. *Nature* **423**, 956–U1 (2003).
3. DeMets, C., Gordon, R. G. & Argus, D. F. Geologically current plate motions. *Geophys. J. Int.* **181**, 1–80 (2010).
4. Ligi, M., Cuffaro, M. , Chierici, F. & Calafato, A. Three-dimensional passive mantle flow beneath mid-ocean ridges: an analytical approach. *Geophys. J. Inter*. **175**, 783–805 (2008).
5. Morgan, J. P. & Forsyth, D. W. Three-dimensional flow and temperature perturbations due to a transform offset: Effects on oceanic crustal and upper mantle structure. *J. Geophys. Res.* **93**, 2955–2966 (1988).
6. Reid, I. & Jackson, H. R. Oceanic spreading rate and crustal thickness. *Mar. Geophys. Res.* **5**, 165–172 (1981).
7. Blackman, D. K. & Forsyth, D. W. The effects of plate thickening on three dimensional passive flow of the mantle beneath mid-ocean ridges. (eds Morgan J. P., Blackman D. K. & Sinton J. M.), *Am. Geophys. Monogr*. **71**, 311–326 (1992).
8. Shen, Y. & Forsyth, D. W. The effects of temperature and pressure dependent viscosity on three-dimensional passive flow of the mantle beneath a ridge-transform system. *J. Geophys. Res*. **97**, 19717–19728 (1992).
9. Buck, W. R. & Su, W. Focused mantle upwelling below mid-ocean ridges due to feedback between viscosity and melting. *Geophys. Res. Lett.* **16**, 641–644 (1989).
10. Scott, D. R. & Stevenson, D. J. A self-consistent model of melting, magma migration and buoyancy-driven circulation beneath mid-ocean ridges. *J. Geophys. Res.* **94**, 2973–2988 (1989).
11. Sotin, C. J. & Parmentier, E. M. Dynamical consequences of compositional and thermal density stratification beneath spreading centers. *Geophys. Res. Lett.* **16**, 835–838 (1989).
12. Ligi, M., Bonatti**,** E., Cipriani, A. & Ottolini, L. Water-rich basalts at mid-ocean-ridge cold spots. *Nature* **434**, 66–69 (2005).
13. Katz, R. F., Spiegelman, M. & Langmuir, C. H. A new parameterization of hydrous mantle melting. *Geochem. Geophys. Geosyst.* **4,** 1073 (2003).
14. Hirth, G. & Kohlstedt, D. L. Water in the oceanic upper mantle: Implications for rheology, melt extraction and the evolution of the lithosphere. *Earth Planet. Sci. Lett.* **144**, 93–108 (1996).

15. McKenzie, D. & O'Nions, R. K. Partial Melt distributions from inversion of rare Earth Elements concentrations. *J. Petrol.* **32**, 1021–1091 (1991).

16. Hellebrand, E., Snow, J. E., Hoppe, P. & Hofmann, A. W. Garnet-field melting and Late-stage Refertilization in "Residual" Abyssal Peridotites from the Central Indian Ridge. *J. Petrol.* **43**, 2305–2338 (2002).

17. Asimow, P. D. & Langmuir, C. H. The importance of water to oceanic mantle melting regimes, *Nature* **421**, 815–820 (2003).

18. Chen, Y. J. Oceanic crustal thickness versus spreading rate, *Geophys. Res. Lett.*, **19**, 753–756 (1992).

19. Klingelhöfer, F., Géli, L., Matias, L., Steinsland, N. & Mohr, J. Crustal structure of a super-slow spreading centre: a seismic study of Mohns Ridge, 72°N. *Geophys. J. Int.* **141**, 509–526 (2000).

20. White, R. S., Minshull, T. A., Bickle, M. J. & Robinson, C. J. Melt generation at very slow-spreading oceanic ridges: constraints from geochemical and geophysical data. *Journal of Petrology* **42**, 1171–1196 (2001).

21. Jokat, W. & Schmidt-Aursch, M. C. Geophysical characteristics of the ultraslow spreading Gakkel Ridge, Arctic Ocean. *Geophys. J. Int.* **168**, 983–998 (2007).

22. Holmes, R. C., Tolstoy, M., Cochran, J. R. & Floyd, J. S. Crustal thickness variations along the Southeast Indian Ridge (100°–116°E) from 2-D body wave tomography. *Geochem. Geophys. Geosyst.* **9**, Q12020, doi:10.1029/2008GC002152 (2008).

23. Iyer, K., Rüpke, L. H. & Morgan, J. P. Feedbacks between mantle hydration and hydrothermal convection at ocean spreading centers. *Earth Planet. Sci. Lett.* **296**, 34–44 (2010).

24. Bonatti, E., Ligi, M., Brunelli, D., Cipriani, A., Fabretti, P., Ferrante, V., Gasperini, L. & Ottolini, L. Mantle thermal pulses below the Mid-Atlantic Ridge and temporal variations in the formation of oceanic lithosphere. *Nature* **423**, 499-505 (2003).

25. Boschi, C. La formazione di litosfera oceanica nell'Atlantico Equatoriale: le serpentiniti della Vema Fracture Zone. Msc Thesis, University of Pisa (2000).

26. Brunelli, D., Seyler, M., Cipriani, A., Ottolini, L. & Bonatti, E. Discontinuous melt extraction and weak refertilization of mantle peridotites at the Vema lithospheric section (Mid-Atlantic Ridge). *Journal of Petrology* **47**, 745–771 (2006).

27. Snow, J. E. & Dick, H. J. B. Pervasive magnesium loss by marine weathering of peridotite. *Geochim. Cosmochim. Acta*, **59**, 4219-4235 (1995).

28. Hamlyn, P. R. & Bonatti, E. Petrology of mantle-derived ultramafics from the Owen fracture zone, northwest Indian ocean: Implications for the nature of the oceanic upper mantle. *Earth Planet. Sci. Lett.* **48**, 65–79 (1980).

29. Dick, H. J. B. Abyssal peridotites, very slow spreading ridges and ocean ridge magmatism. *Geol. Soc. London, Special Publications* **42**, 71-105 (1989).

30. Fujii, T. Petrology of peridotites from HOLE 670A, LEG 109. *Proc. ODP, Sci. Results* **106/109**, 19–25 (1990).

31. Komor, S. C., Grove, T. L. & Hebert, R. Abyssal peridotites from ODP HOLE 670A (21° 10' N, 45°02' W): residues of mantle melting exposed by non-constructive axial divergence. *Proc. ODP, Sci. Results* **106/109**, 85–101 (1990).

32. Johnson, K. T. M. & Dick, H. J. B. Open System Melting and Temporal and Spatial Variation of Peridotite and Basalt at the Atlantis II Fracture Zone. *J. Geophys. Res.* **97**, 9219–9241(1992).

33. Cannat, M. & Casey, J. F. An ultramafic lift at the Mid-Atlantic Ridge: successive stages of magmatism in serpentinized oceanic upper mantle: Mid-Atlantic Ridge 15° N. (eds Vissers, R. L. M. & Nicolas, A.) Mantle and lower crust exposed in oceanic ridges and in ophiolites, *Kluwer Academic Publisher*, 5–34 (1995).

34. Edwards, S. J., Malpas, J. Melt-peridotite interactions in shallow mantle at the East Pacific Rise: Evidence from ODP SITE 895 (Hess Deep). *Mineralog. Mag.* **60**, 191–206 (1996).

35. Ghose, I., Cannat, M. & Seyler, M. Transform fault effect on mantle melting in the MARK area (Mid-Atlantic Ridge south of the Kane transform). *Geology* **24**, 1139–1142 (1996).

36. Ross, K. & Elthon, D. Extreme incompatible trace-element depletion of diopside in residual mantle from South of the Kane Fracture Zone. *Proc. ODP, Sci. Results* **153**, 277–284 (1997).

37. Burgath, K. P., Marchig, V. & Mussallam, K. Data report: mineralogic, structural and chemical variability of mantle sections from HOLES 920B and 920D. *Proc. ODP, Sci. Results* **153**, 505–521 (1997).

38. Ohara, Y. & Stern, R., Ishii, T., Yurimoto, H. & Yamazaki, T. Peridotites from the Mariana Trough: first look at the mantle beneath an active back-arc basin. *Contrib. Mineral. Petrol.* **143**, 1–18 (2002).

39. Brunelli, D., Cipriani, A., Ottolini, L., Peyve, A. & Bonatti, E. Mantle peridotites from the Bouvet Triple Junction Region, South Atlantic. *Terra Nova* **15**, 194–203 (2003).

40. Seyler, M., Cannat, M. & Mével, C. Evidence for major-element heterogeneity in the mantle source of abyssal peridotites from the Southwest Indian Ridge (52° to 68°E), *Geochem. Geophys. Geosyst.* **4**, 9101, doi:10.1029/2002GC000305 (2003).

41. Coogan, L. A., Thompson, G. M., MacLeod, C. J., Dick, H. J. B., Edwards, S. J., Scheirer, A. H. & Barry, T. L. A combined basalt and peridotite perspective on 14 million years of melt generation at the Atlantis Bank segment of the Southwest Indian Ridge: evidence for temporal changes in mantle dynamics?. *Chemical Geology* **207**, 13–30 (2004).

42. Seyler, M., J.-P. Lorand, Dick, H. J. B. & Drouin, M. Pervasive melt percolation reactions in ultra-depleted refractory harzburgites at the Mid-Atlantic Ridge, 15° 20′N: ODP Hole 1274A. *Contrib. Mineral. Petrol.* **153**, 303–319 (2007).

43. Warren, J. M., Shimizu, N., Sakaguchi, C., Dick, H. J. B. & Nakamura, E. An assessment of upper mantle heterogeneity based on abyssal peridotite isotopic compositions, *J. Geophys. Res.* **114**, B12203, doi:10.1029/2008JB006186 (2009).

44. Dick, H. J. B., Lissenberg, C. J. & Warren, J. M. Mantle Melting, Melt Transport, and Delivery Beneath a Slow-Spreading Ridge: The Paleo-MAR from 23°15′N to 23°45′N. *J. Petrol.* **51**, 425–467 (2010).

45. Kominz, M. A. Oceanic ridge volume and sea-level change - An error analysis. (ed. Schlee, J. S.), *AAPG Memoir* **36**, 109–127 (1984).

46. Gaffin, S. Ridge volume dependence on seafloor generation rate and inversion using long term sea level change. *Am. J. Sci.* **287**, 596–611 (1987).

47. Berner, R. A. & Kothavala, Z. GEOCARB III: A revised model of atmospheric CO_2 over Phanerozoic time. *Am. J. Sci.* **301**, 182–204 (2001).

48. Hardie, L.A, Secular variation in seawater chemistry: An explanation for the coupled secular variation in the mineralogies of marine limestones and potash evaporites over the past 600 m.y. *Geology* **24**, 279–283 (1996).

49. Cogné, J. P. & Humler, E. Temporal variation of oceanic spreading and crustal production rates during the last 180 My. *Earth Planet. Sci. Lett.* **227**, 427–439 (2004).

50. Rowley, D. B. Rate of plate creation and destruction: 180 Ma to present. *Geol. Soc. Am. Bull.* **114**, 927–933 (2002).

51. Müller, R. D., Roest, W. R., Royer, J.-Y. & Gahagan, L. M. Digital isochrones of the world's ocean floor. *J. Geophys. Res.* **102**, 3211–3214 (1997).

52. Müller, R. D., Sdrolias, M., Gaina, C. & Roest, W. R. Digital isochrones of the world's ocean floor. *Geochem. Geophys. Geosyst.* **9**., doi:10.1029/2007GC001743 (2008).

53. Seton, M., Müller, R. D., Zahirovic, S., Gaina, C., Torsvik, T., Shephard, G., Talsma, A., Gurnis, M., Turner, M., Maus, S. & Chandler, M. Global continental and ocean basin reconstructions since 200 Ma. *Earth Sci. Rev.* **113**, 212–270 (2012).

54. Müller, R. D., Sdrolias, M., Gaina, C., Steinberger, B. & Heine, C. Long-term sealevel fluctuations driven by ocean basin dynamics. *Science* **319**, 1357–1362 (2008).

55. Becker, T. W., Conrad, P. C., Buffett, B. A. & Muller, R. D. Past and present seafloor age distributions and the temporal evolution of plate tectonic heat transport. *Earth Planet. Sci. Lett.* **278**, 233–242 (2009).

56. Wilkinson, B. H. & Algeo, T. J. Sedimentary carbonate record of calcium-magnesium cycling. *Am. J. Sci.* **289**, 1158–1194 (1989).

57. Hansen, K. W. & Wallmann, K. Cretaceous and Cenozoic evolution of seawater composition, atmospheric O2 and CO2: a model perspective. *Am. J. Sci.* **303**, 94–148 (2003).

58. Berner, R. A. A model for calcium, magnesium, and sulfate in seawater over Phanerozoic time. *Am. J. Sci.* **304**, 438–453 (2004).

59. Holland, H. D. Sea level, sediments and the composition of seawater, *Am. J. Sci.* **305**, 220–239 (2005).

60. Demicco, R. V., Lowenstein, T. K., Hardie, L. A. & Spencer, R. J. Model of seawater composition for the Phanerozoic. *Geology* **33**, 877–880 (2005).

61. Zimmerman, H. Tertiary seawater chemistry: implications from primary fluid inclusions in marine halite. *Am. J. Sci.* **300**, 723–767 (2000).

62. Lowenstein, T. K., Timofieff, M. N., Brennan, S. T., Hardie L. A. & Demicco, R. M. Oscillations in Phanerozoic seawater chemistry: evidence from fluid inclusions. *Science* **294**, 1086–1088 (2001).

63. Horita J., Zimmermann H. & Holland H. D. Chemical evolution of seawater during the Phanerozoic: implications from the record of marine evaporites. *Geochim. Cosmochim. Acta* **66**, 3733–3756 (2002).

64. Timofeeff, M. N., Lowenstein, T. K., da Silva, M. A. M & Harris, N. B. Secular variation in the major-ion chemistry of seawater: Evidence from fluid inclusions in Cretaceous halites. *Geochim. Cosmochim. Acta* **70**, 1977–1994 (2006).

65. Fantle, M. S. & DePaolo, D. J. Sr isotopes and pore fluid chemistry in carbonate sediment of the Ontong Java Plateau: Calcite recrystallization rates and evidence for a rapid rise in seawater Mg over the last 10 million years. *Geochim. Cosmochim. Acta* **70**, 3883–3904 (2006).

66. Lear, C. H., Elderfield, H. & Wilson, P. A. Cenozoic deep‐sea temperature and global ice volumes from Mg/Ca in benthic foraminiferal calcite. *Science* **287**, 269–272 (2000).

67. Dickson, J. A. D. Fossil echinoderms As monitor of the Mg/Ca ratio of phanerozoic oceans. *Science* **298**, 1222–1224 (2002).

68. Steuber, T. & Rauch, M. Evolution of the Mg/Ca ratio of Cretaceous seawater: Implications from the composition of biological low Mg calcite. *Mar. Geol.* **217**, 199–213 (2005).

69. Coggon, R. M., Teagle, A. H. D., Smith-Duque, C. E., Alt, J. C. & Cooper., M. J. Reconstructing past seawater Mg/Ca and Sr/Ca from mid-Ocean Ridge flank calcium carbonate veins. *Science* **327**, 1114–1117 (2010).

70. Paytan, A., Kastner, M., Campbell, D. M. & Thiemens, H. Seawater sulfur isotope fluctuations in the Cretaceous. *Science* **304**, 1663–1665 (2004).

71. Tipper, E. T., Galy, A., Gaillardet, J., Bickle, M. J., Elderfield, H. & Carder, E. A. The magnesium isotope budget of the modern ocean: constraints from riverine magnesium isotope ratios. *Earth Planet. Sci. Lett.* **250**, 241–253 (2006).

72. Paris, G., Gaillardet, J. & Louvat, P. Geological evolution of seawater boron isotopic composition recorded in evaporates. *Geology* **38**, 1035–1038 (2010).

73. Wortmann, U. G. & Paytan, A. Rapid Variability of Seawater Chemistry Over the Past 130 Million Years. *Science* **337**, 334–336 (2012).

74. Mottl, M. J. & Wheat, C. G. Hydrothermal circulation through midocean ridge flanks: Fluxes of heat and magnesium. *Geochim. Cosmochim. Acta* **58**, 2225–2237 (1994).

75- Elderfield, H., Wheat, G. C., Mottl, M. J., Monnin, C. & Spiro, B. Fluid and geochemical transport through ocean crust: A transect across the eastern flank of the Juan de Fuca Ridge. *Earth Planet. Sci. Lett.* **172**, 151–165 (1999).

76. Wheat, C. G. & Mottl, M. J. Composition of pore and spring waters from Baby Bare: Global implications of geochemical fluxes from a ridge flank hydrothermal system. *Geochim. Cosmochim. Acta* **64**, 629–642 (2000).

77. Dick, H. J. B., Lin, J. & Schouten, H. An ultraslowspreading class of ocean ridge. *Nature* **426**, 405–412 (2003).

78. Cannat, M., Mével, C., Maia, M., Deplus, C., Durand, C., Gente, P., Agrinier, P., Belarouchi, A., Dubuisson, G., Humler, E. & Reynolds, J. Thin crust, ultramafic exposures, and rugged faulting patterns at the the Mid-Atlantic Ridge (22°–24°N). *Geology* **23**, 49–52 (1995).

79. Cannat, M., Sauter, D., Bezos, A., Meyzen, C., Humler, E. & Le Rigoleur, M. Spreading rate, spreading obliquity, and melt supply at the ultraslow spreading Southwest Indian Ridge. *Geochem. Geophys. Geosys.* **9**, Q04002. doi:10.1029/2007GC001676 (2008).

80. Smith, D. K., Escartin, J., Schouten, H. & Cann, J. R. Fault rotation and core complex formation: significant processes in seafloor formation at slow-spreading midocean ridges (Mid-Atlantic Ridge, 13–15°N). *Geochem. Geophys. Geosys.* **9**, Q03003. doi:10.1029/2007GC001699 (2008).

81. Escartín, J., Smith, D. K., Cann, J., Schouten, H., Langmuir, C. H. & Escrig, S., Central role of detchment faults in accretion of slow-spreading oceanic lithosphere. *Nature* **455**, 790–794 (2008).

82. Bonatti, E., Lawrence, J. P., Hamlyn, P. R. & Breger, D. Aragonite from deep sea ultramafic rocks. *Geochim. Cosmochim. Acta* **44**, 1207–1214 (1980).

83. Kelley, D. S., Karson, J. A., Blackman, D. K., Fruh-Green, G. L., Butterfield, D. A., Lilley, M. D., Olson, E. J., Schrenk, M. O., Roe, K. K., Lebon, G. T., Rivizzigno, P. & the AT3–60 Shipboard Party. An off-axis hydrothermal vent field near the Mid-Atlantic Ridge at 30°N. *Nature* **412**, 145–149 (2001).

84. Given, R. K. & Wilkinson, B. H. Dolomite abundance and stratigraphic age constraint on rates and mechanisms of Phanerozoic dolostone formation. *J. Sed. Petrology* **57**, 1068–1078 (1987).

85. de Villiers, S., Dickson, J. A. D. & Ellam, R. M. The composition of the continental river weathering flux deduced from seawater Mg isotopes. *Chem. Geol.* **216**, 133–142 (2005).

86. Ligi, M., & Bortoluzzi, G. PLOTMAP: geophysical and geological applications of good standard quality cartographic software. *Computers and Geosciences* **15**, 519–585 (1989).

87. Cande, S. C. & Kent, D. V. Revised calibration of the geomagnetic polarity timescale for the Late Cretaceous and Cenozoic. *J. Geophys. Res.* **100**, 6093–6095 (1995).

88. Gradstein, F. M., Agterberg, F. P., Ogg, J. G., Hardenbol, S., Vanveen, P., Thierry, J. & Huang, Z. H. A Mesozoic time scale. *J. Geophys. Res.* **99**, 24051–24074 (1994).

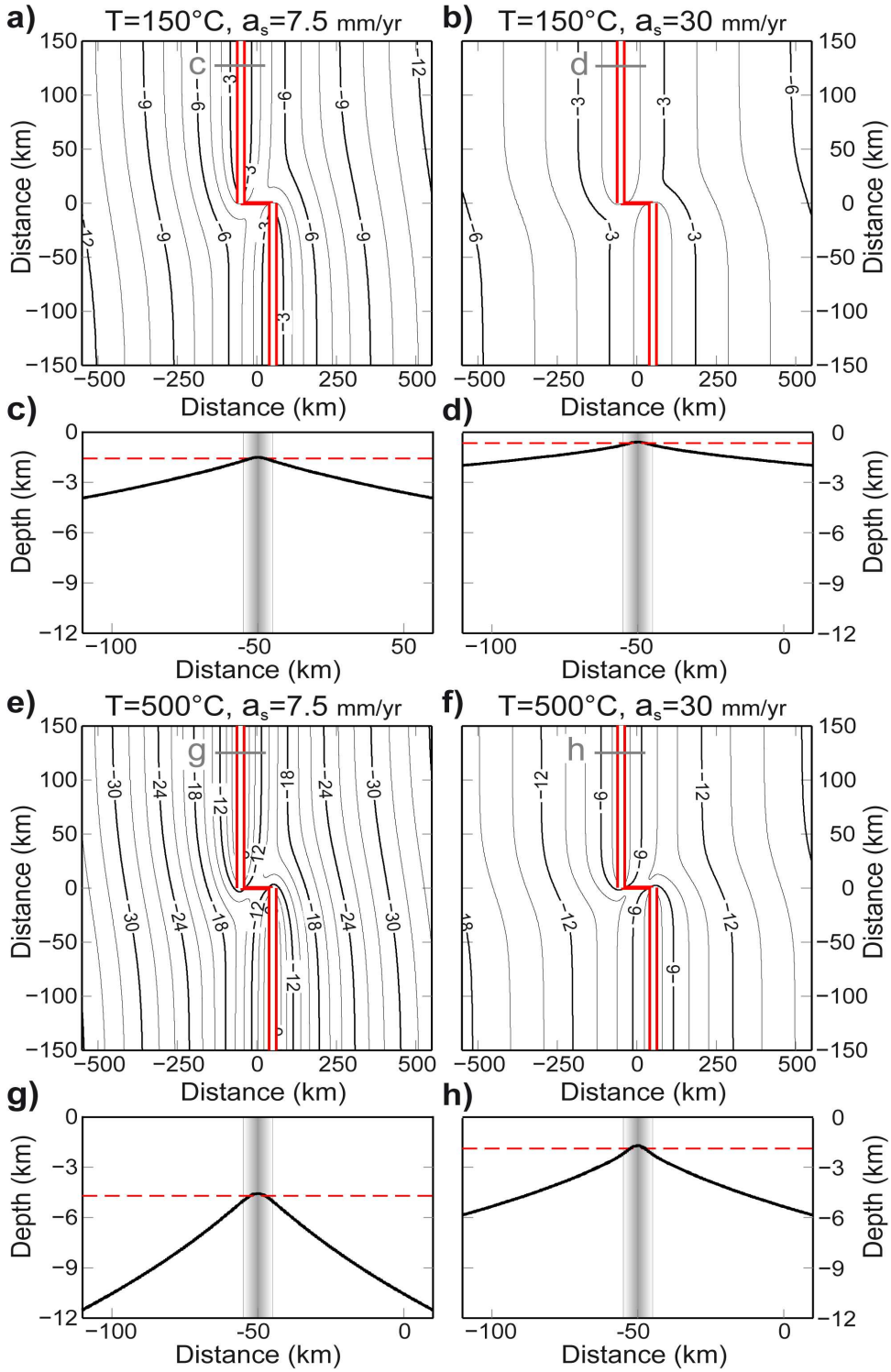

Figure S1. *Mantle thermal structure beneath a ridge-transform-ridge plate boundary and transform offset of 100 km. Depth of 150 °C (**a**, **b**) and 500 °C (**e**, **f**) isotherms for spreading rate of 7.5 and 30.0 mm/yr, respectively. **c**, **d**, **g**, **h**, across axis sections far away from the ridge transform intersection. Red dashed line: mean isotherm depth obtained by averaging depths from the across-axis 10 km-wide region (gray shaded area), where we assume the occurrence of hydrothermal seawater circulation.*

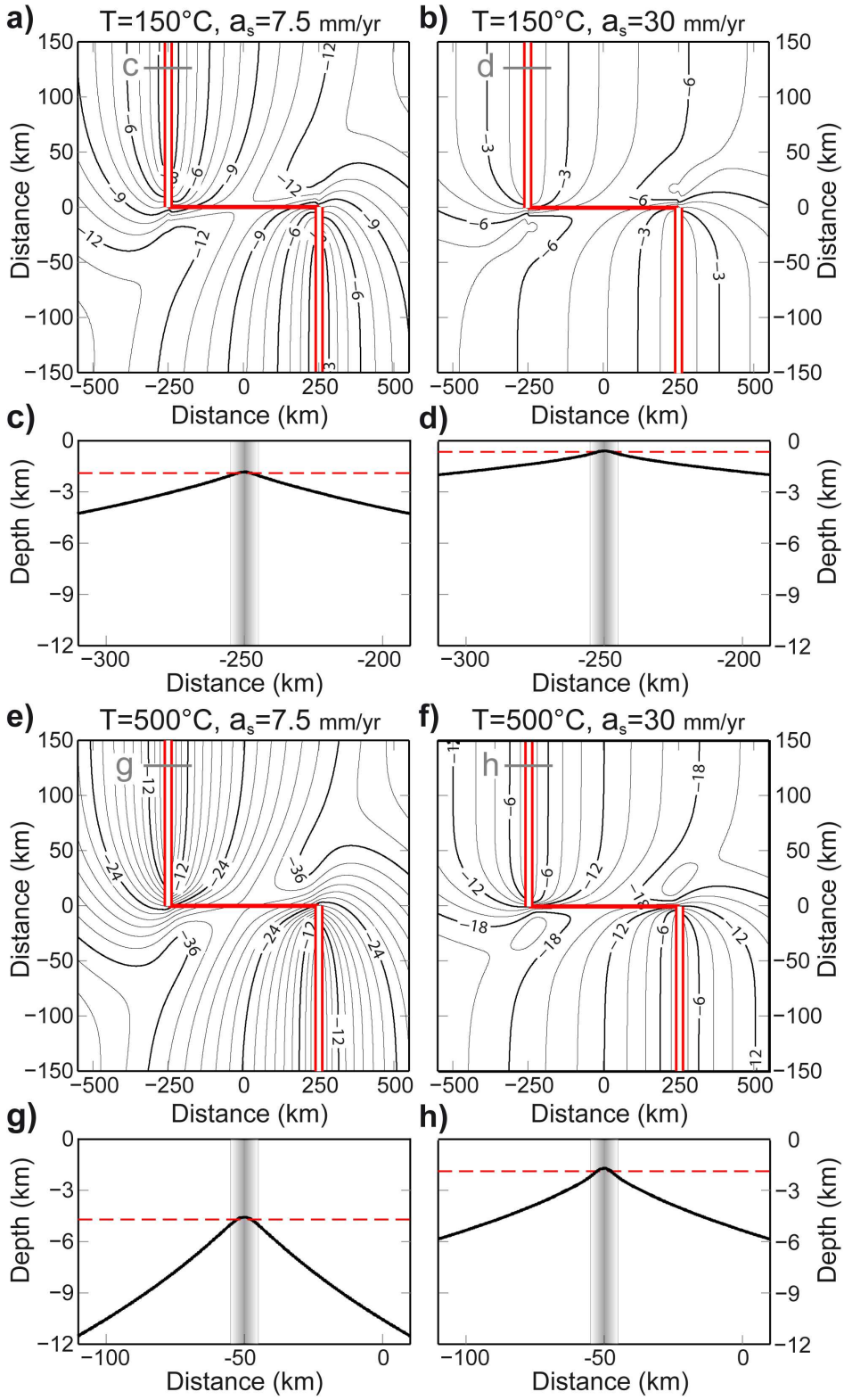

Figure S2. *Mantle thermal structure beneath a ridge-transform-ridge plate boundary and transform offset of 500 km. See caption of figure S1.*

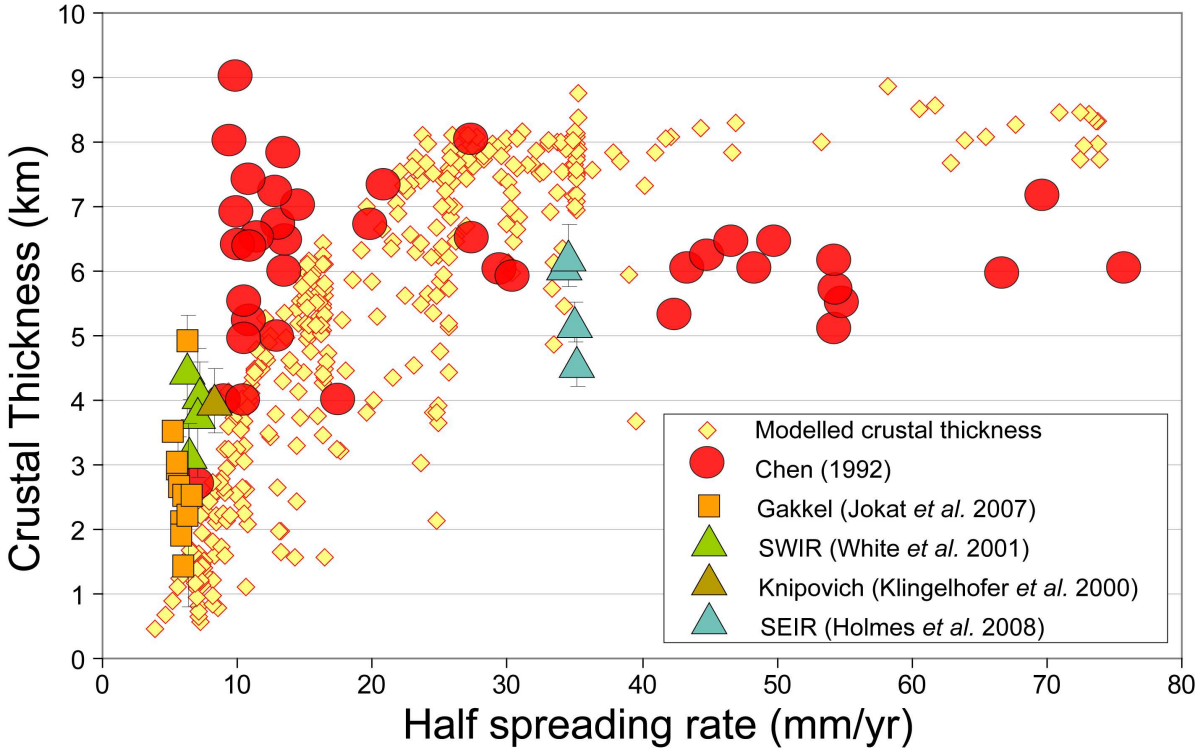

Figure S3. *Oceanic crustal thickness versus spreading rate. Diamonds indicate mean crustal thickness predicted at each mid-ocean ridge segment. Circles, squares and triangles indicate crustal thickness inferred from seismic refraction experiments*[18-22].

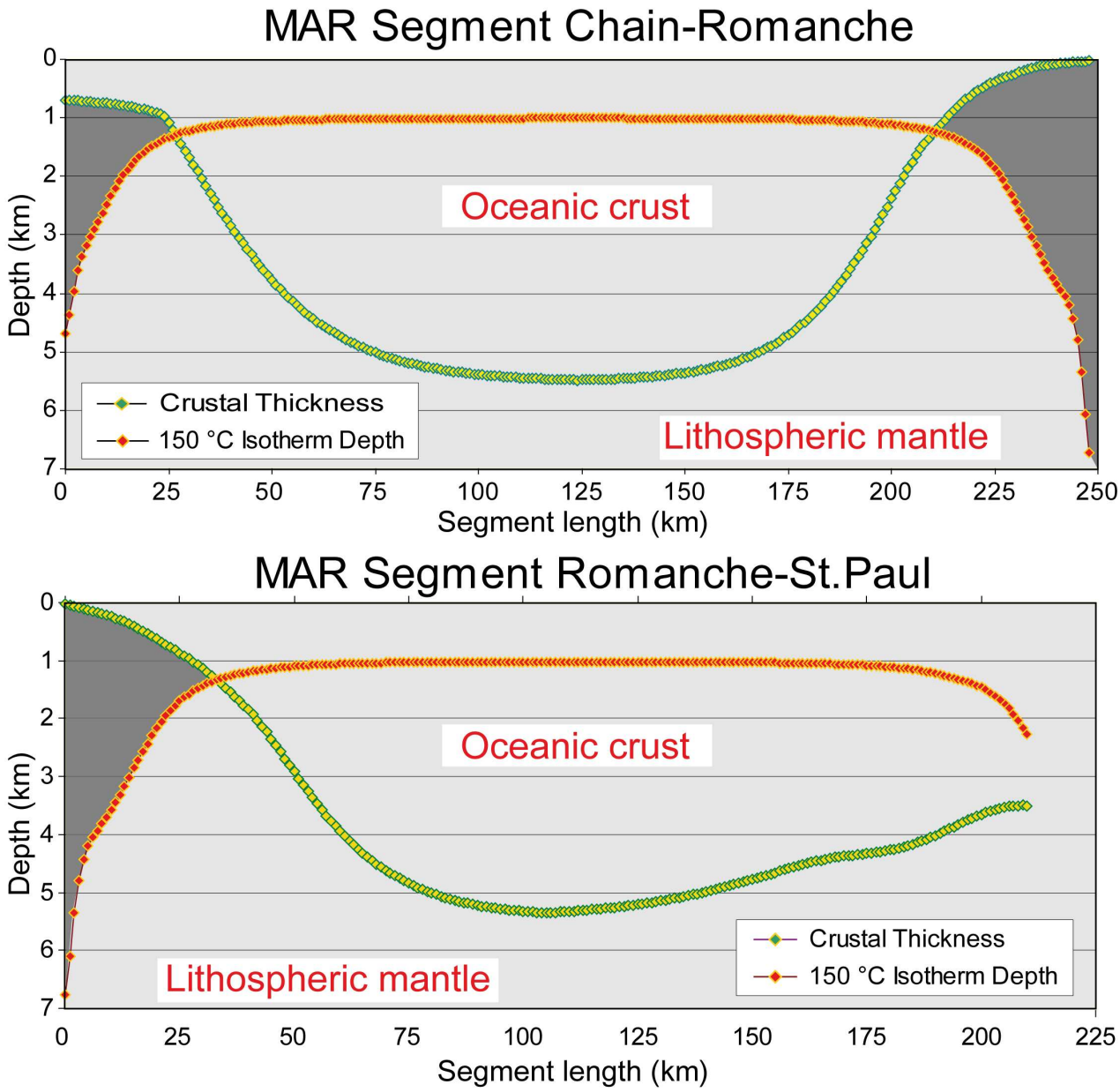

Figure S4. *Crustal thickness and depth from seafloor of the 150 °C isotherm predicted at two Mid Atlantic Ridge segments dislocated by long offset transforms (Chain, Romanche and St. Paul). Shaded areas indicate the mantle region that can contribute to <150 °C MORP-seawater reactions and consequently to Mg release, i.e., the region where the difference between isotherm depth and crustal thickness is positive.*

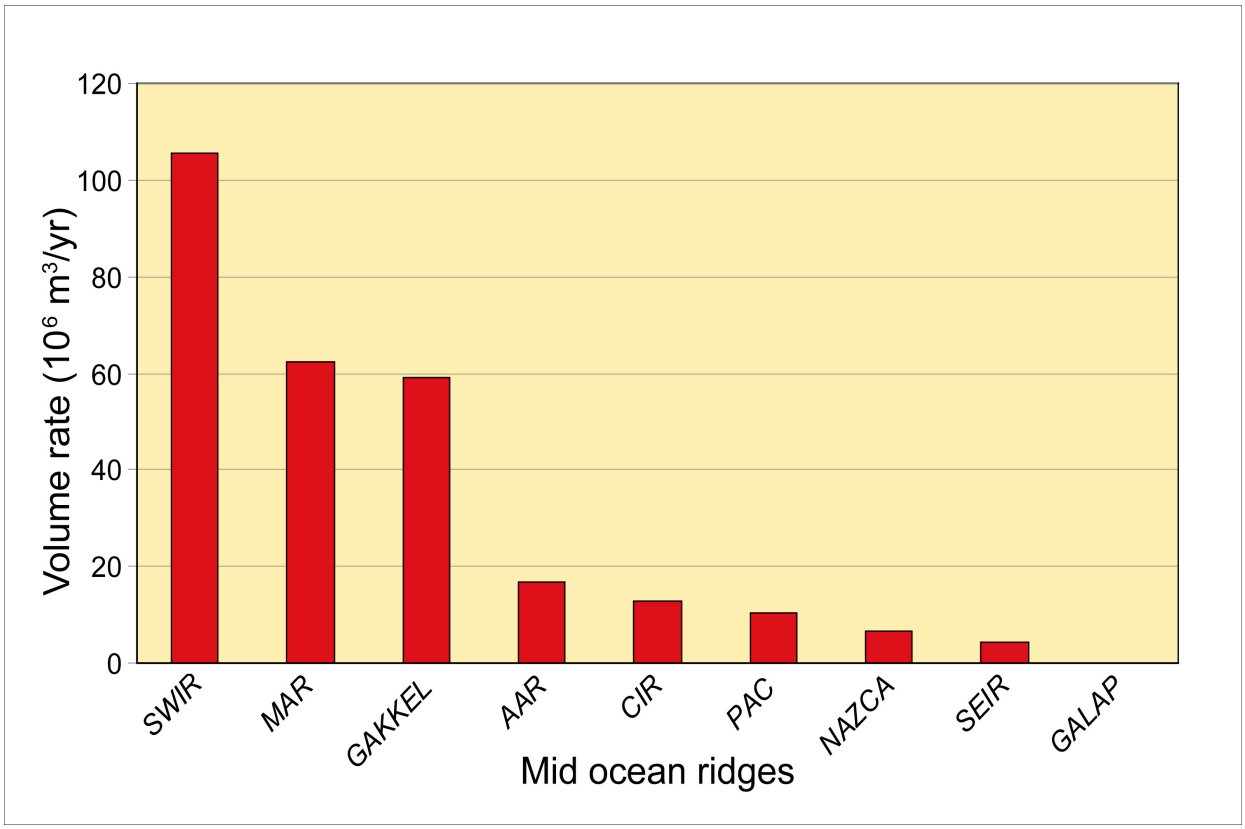

Figure S5. *Volume of mantle rocks that may react with seawater at T <150 °C along present day mid-ocean ridges.*

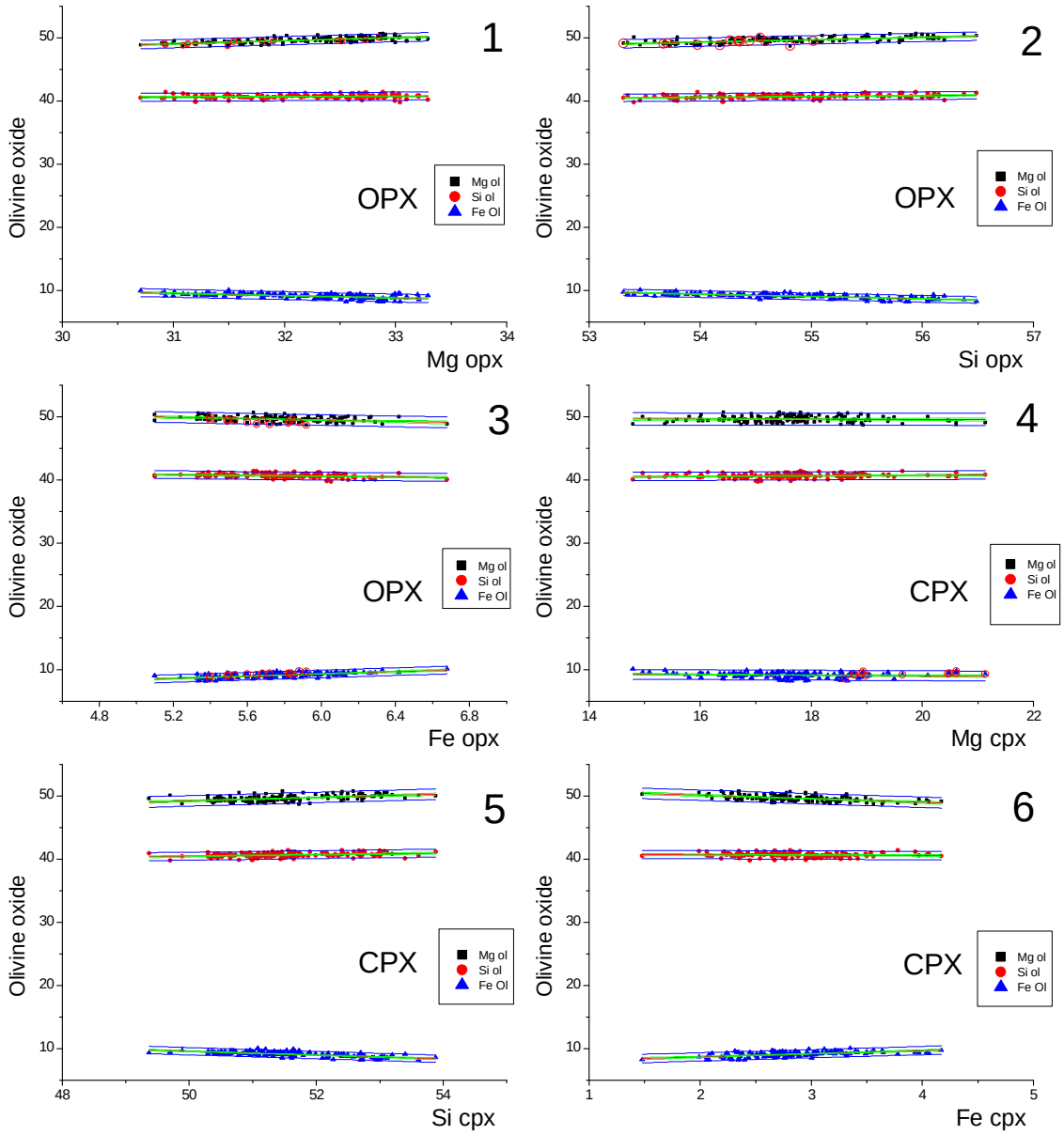

Figure S6. *Linear regression (green solid line) of olivine major oxides (SiO2, MgO and FeO) versus oxides of opx and cpx. 95% confidence intervals are also indicated (gray solid lines).*

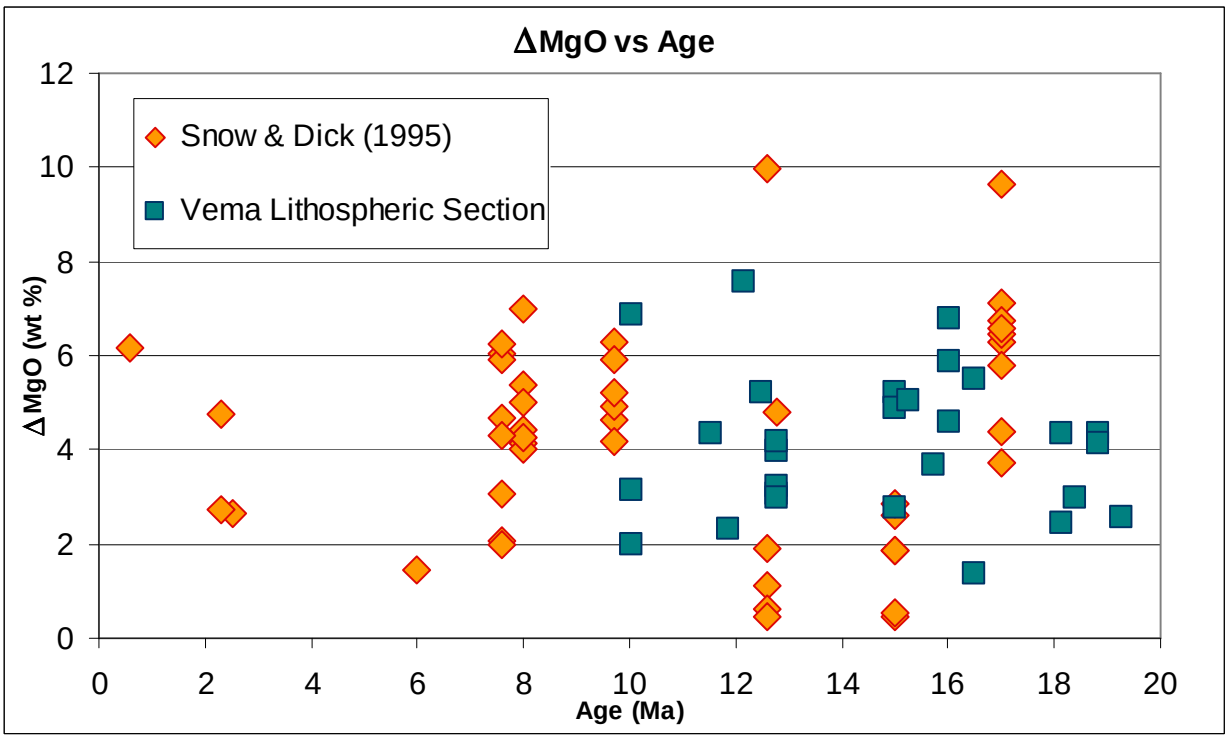

Figure S6. *Mg-loss (ΔMgO) versus crustal age. Diamonds refer to SWIR peridotites*[27]*, squares to Vema Lithosperic Section peridotites*[24-26]*. Both populations show Mg-loss in serpentinites compared to unaltered primary rocks.*

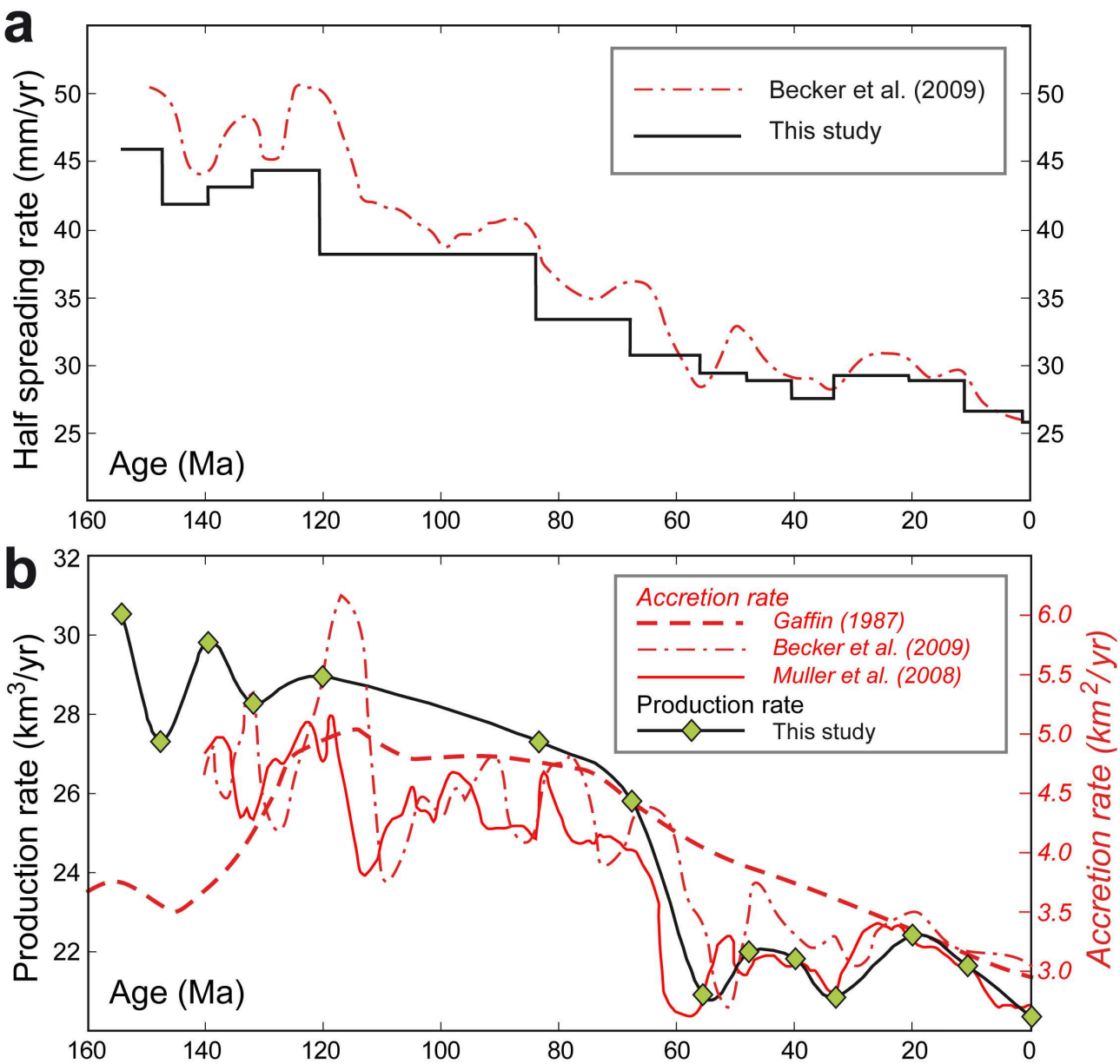

Figure S8. *Spreading rate* ***(a)*** *and oceanic crustal production* ***(b)*** *temporal variations since 150 Ma.*

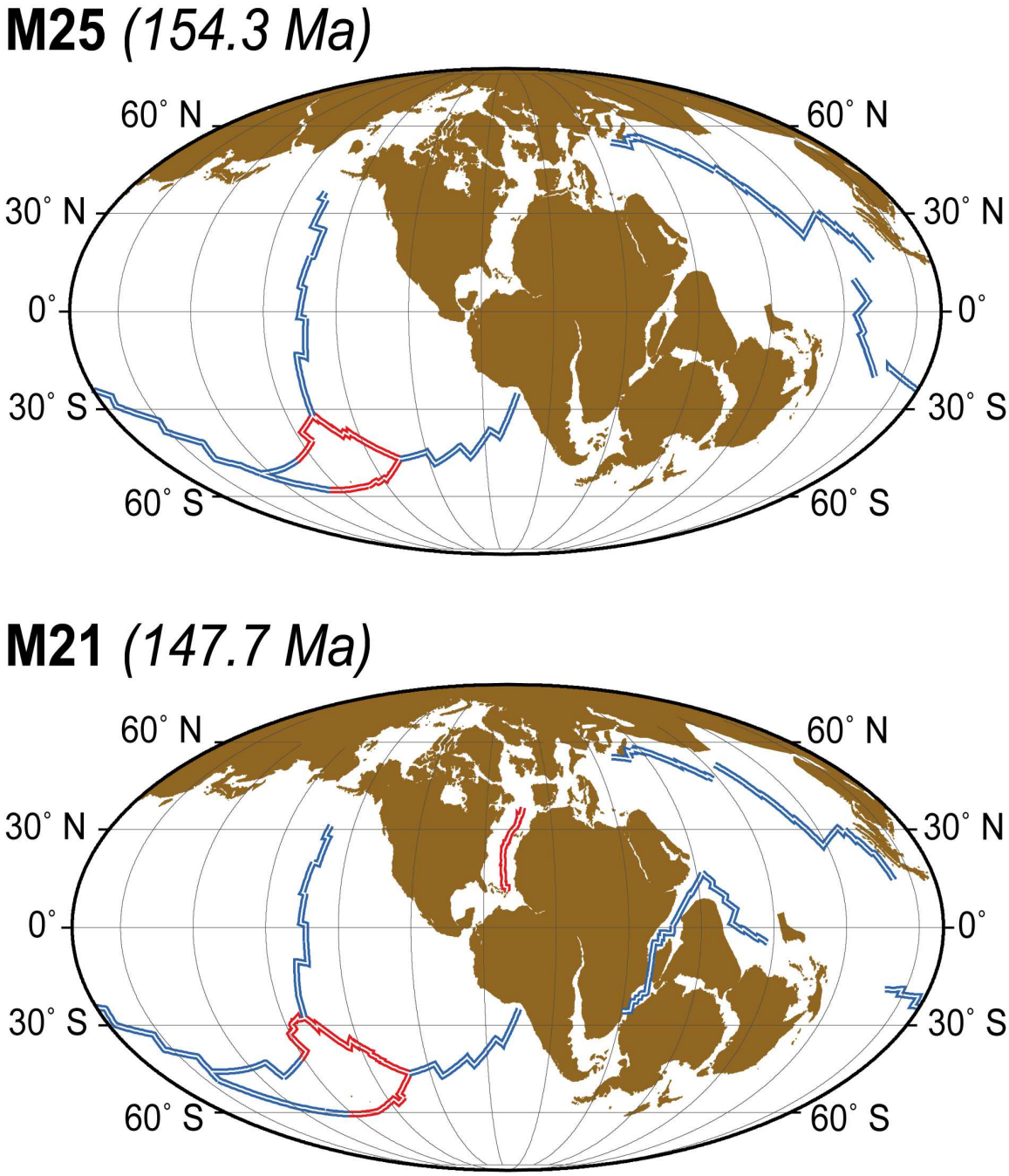

Figure S9. *Global plate reconstructions relative to Africa-fixed reference frame from Late Oxfordian (154 Ma) to the present day. Positions of continents and mid-ocean ridges, obtained with Gplates software (http://www.gplates.org), are plotted in Mollweide projection using PLOT-MAP package[86]. Preserved mid-ocean ridges (double red lines) are from ref. 52, and reconstructed mid-ocean ridges (double blue lines) are from ref. 53. Half spreading rates are calculated by stage poles obtained from the finite Euler poles and rotation angles of ref. 53. Magnetic chron ages (o=lower and y=upper boundary) are from ref. 87 (Chrons 0-34) and ref. 88 (Chrons M25-M0).*

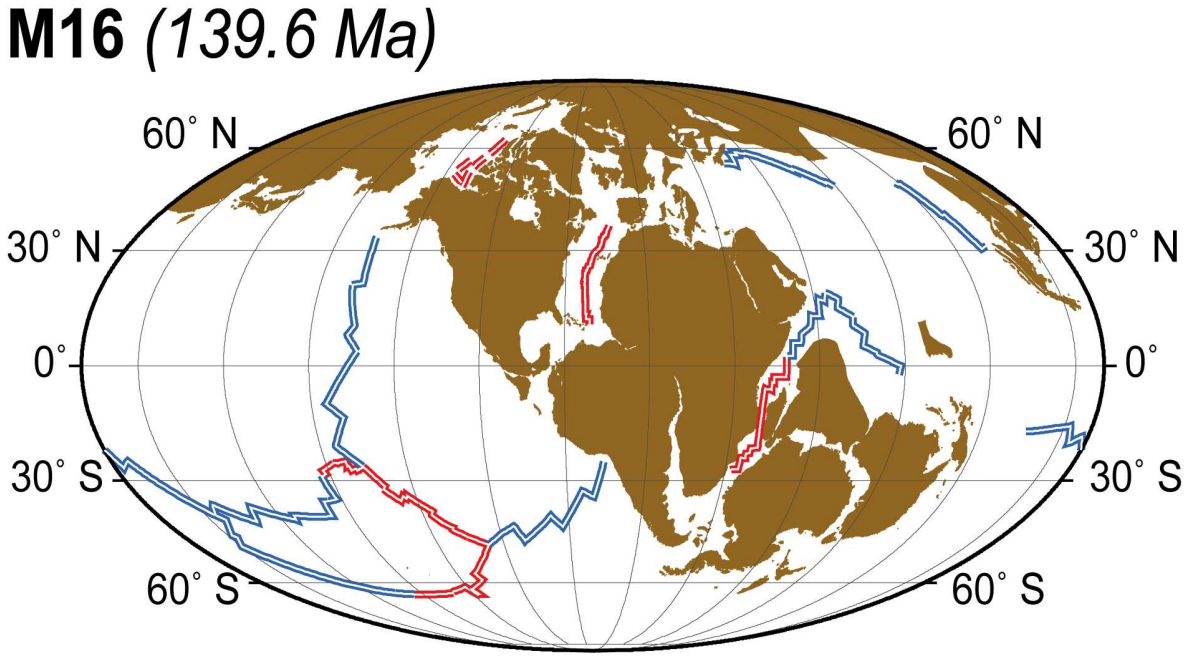

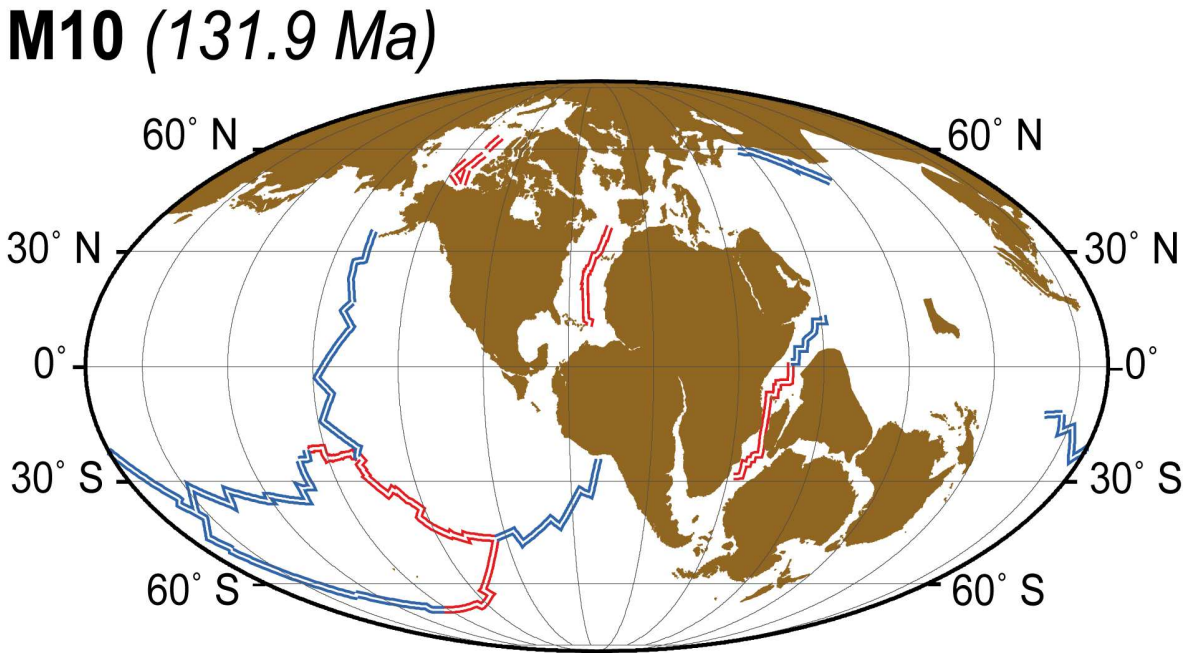

Figure S9 continues.

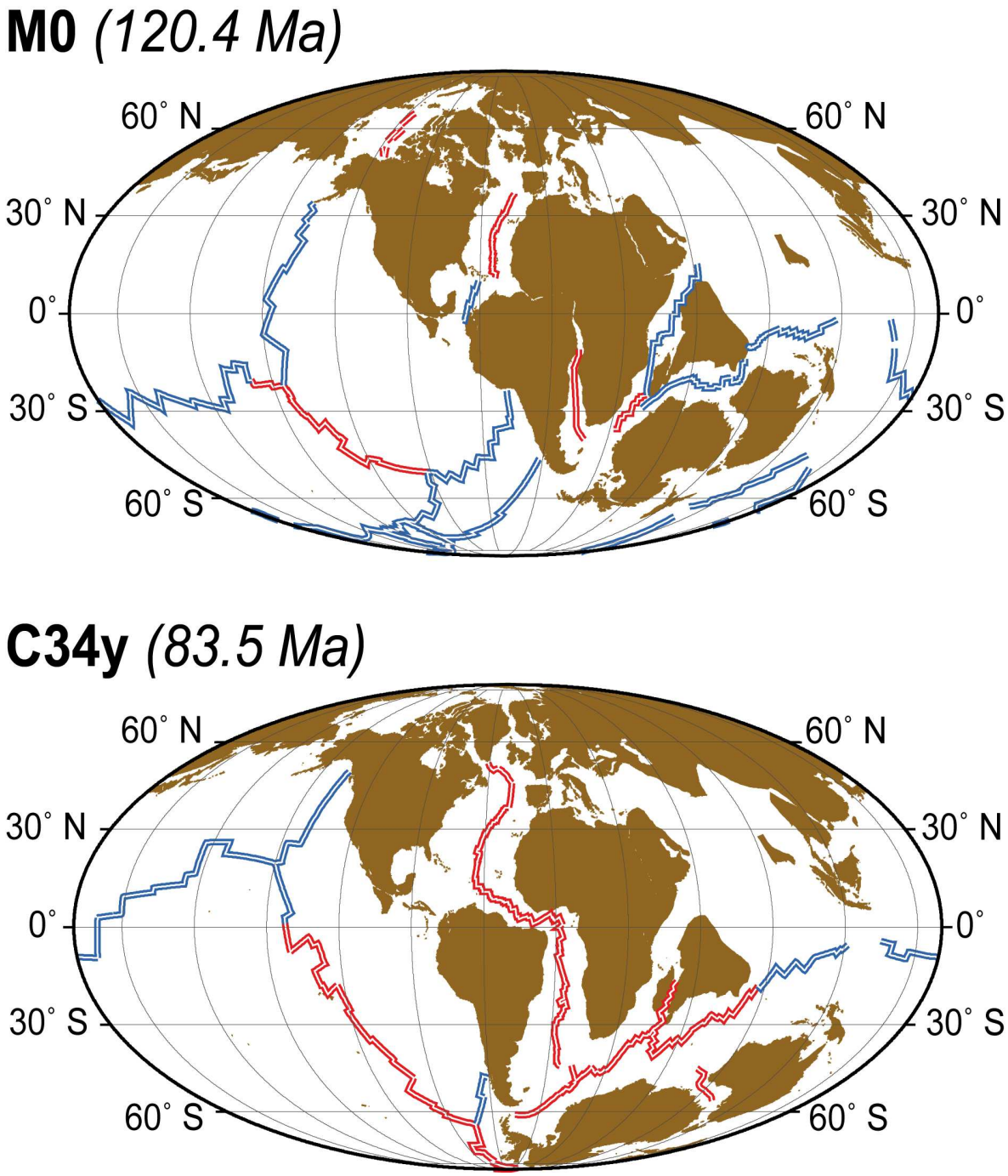

Figure S9 continues.

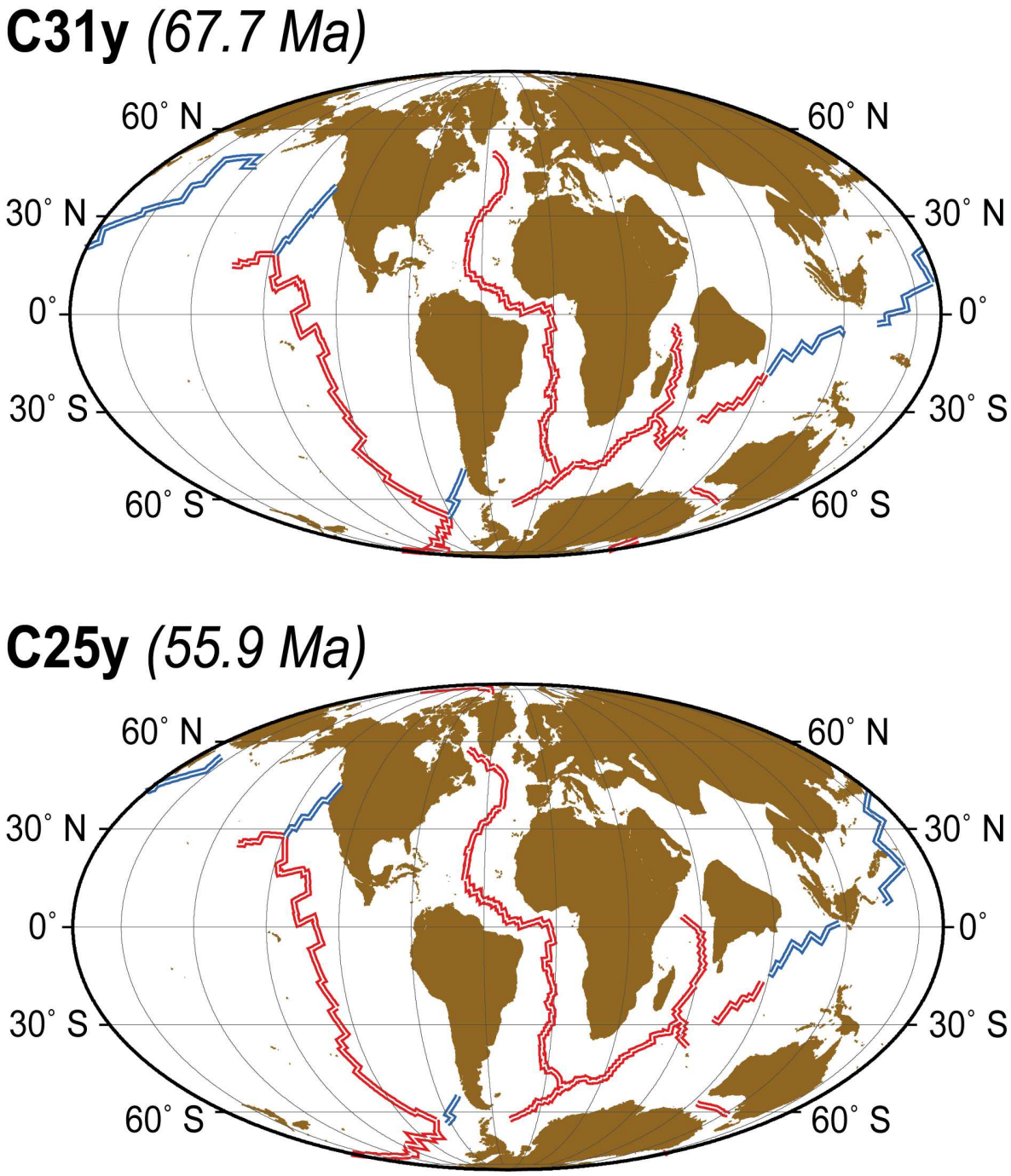

Figure S9 continues.

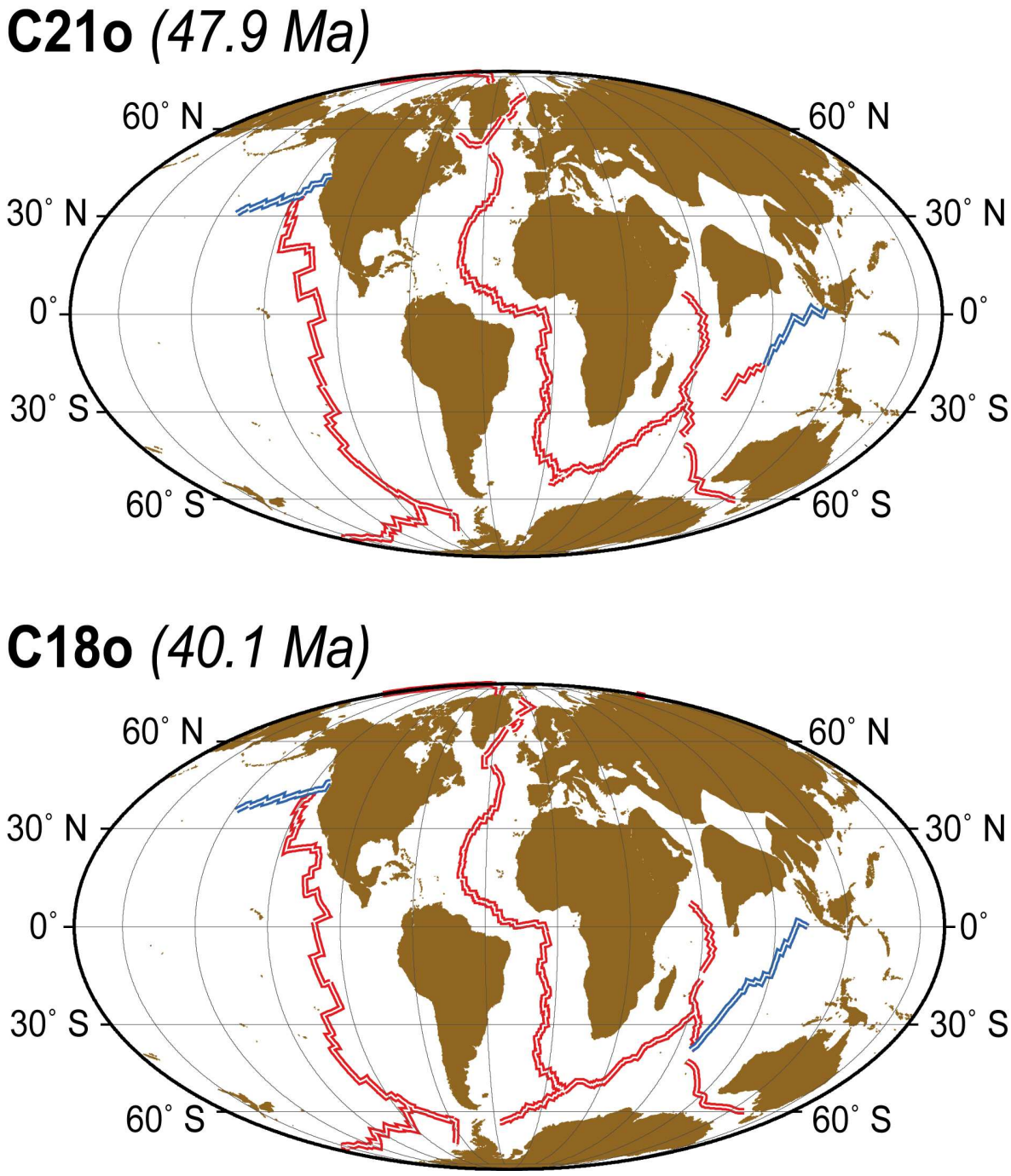

Figure S9 continues.

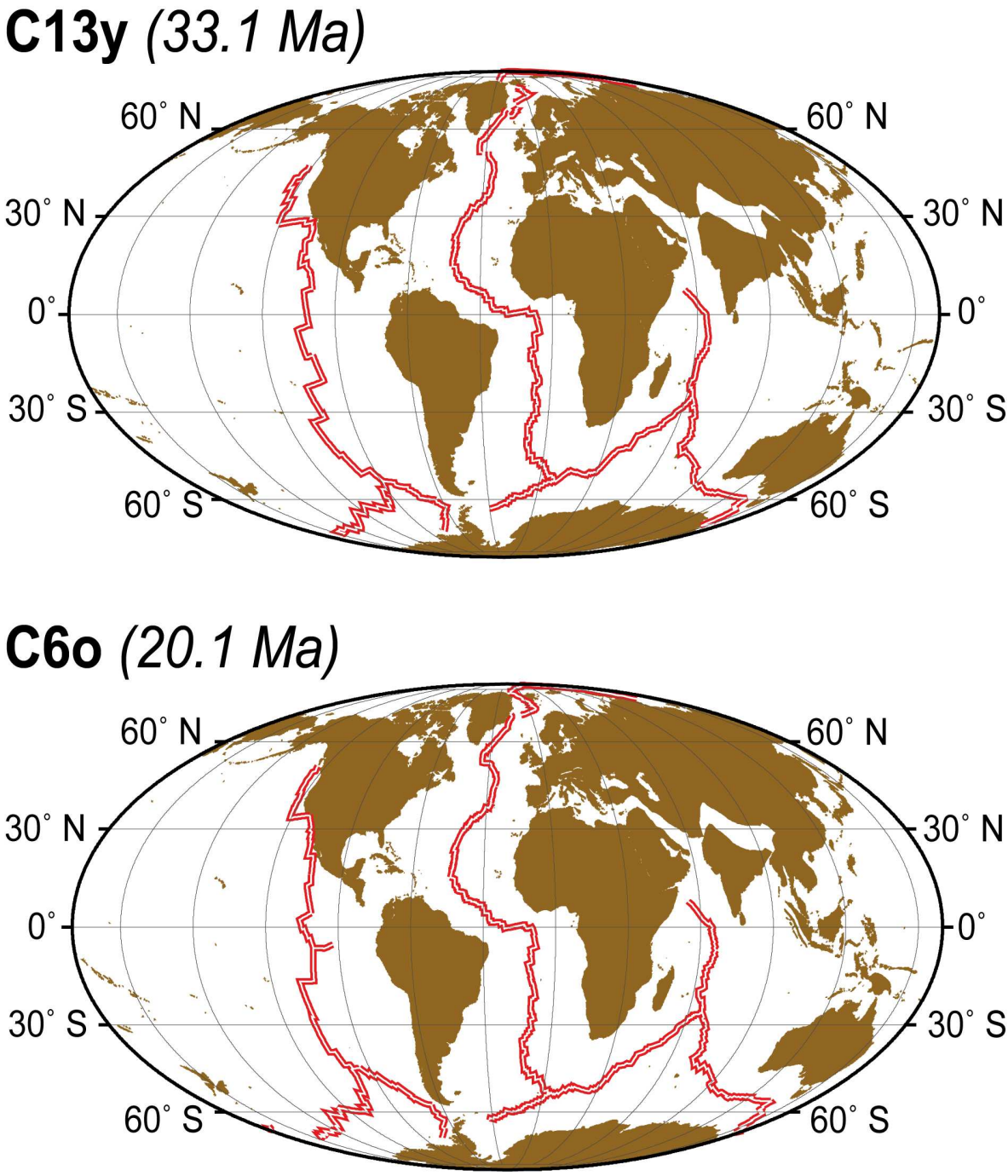

Figure S9 continues.

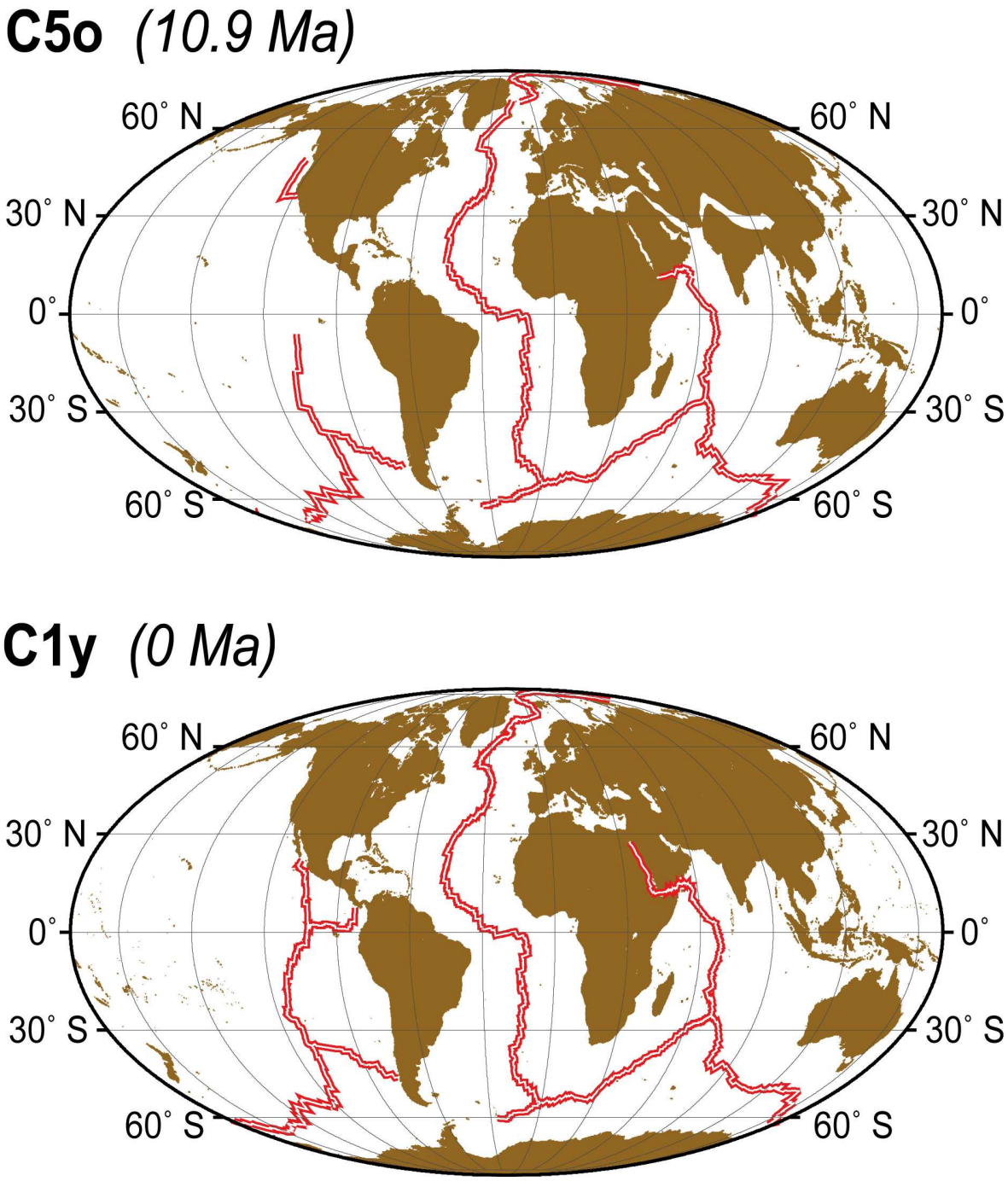

Figure S9 continues.

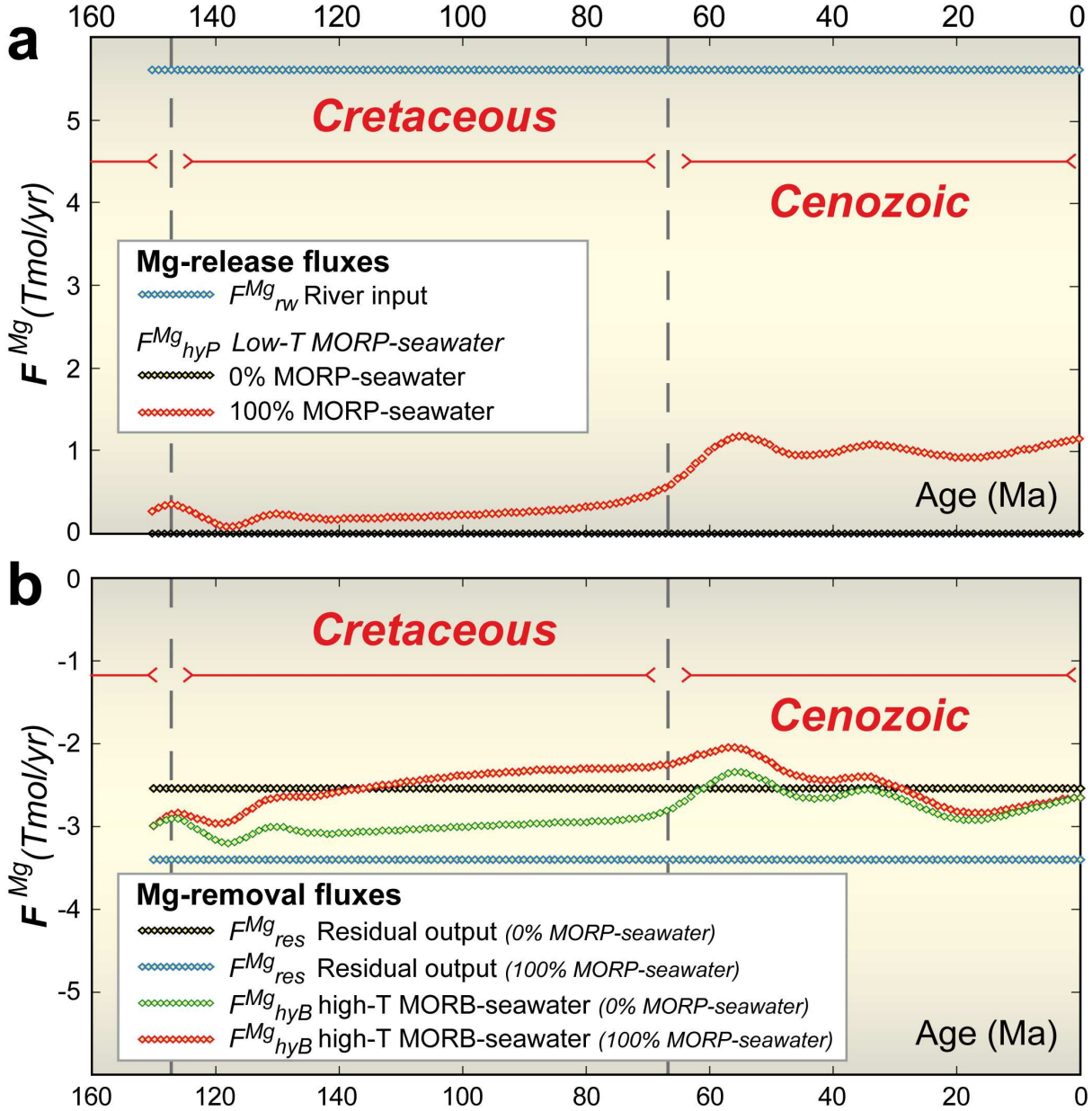

Figure S10. *Modeled seawater Mg fluxes since 150 Ma.* ***a,*** *constant river inflow and temporal variations of Mg-release flux due to low-T MORP-seawater interactions for different volumes of mantle rocks that can interact yearly with seawater at T < 150 °C.* ***b,*** *calculated residual removal flux and temporal changes of Mg-removal flux by high-T hydrothermal circulation in basalts for different volumes of mantle rocks that can interact yearly with seawater at T < 150 °C.*

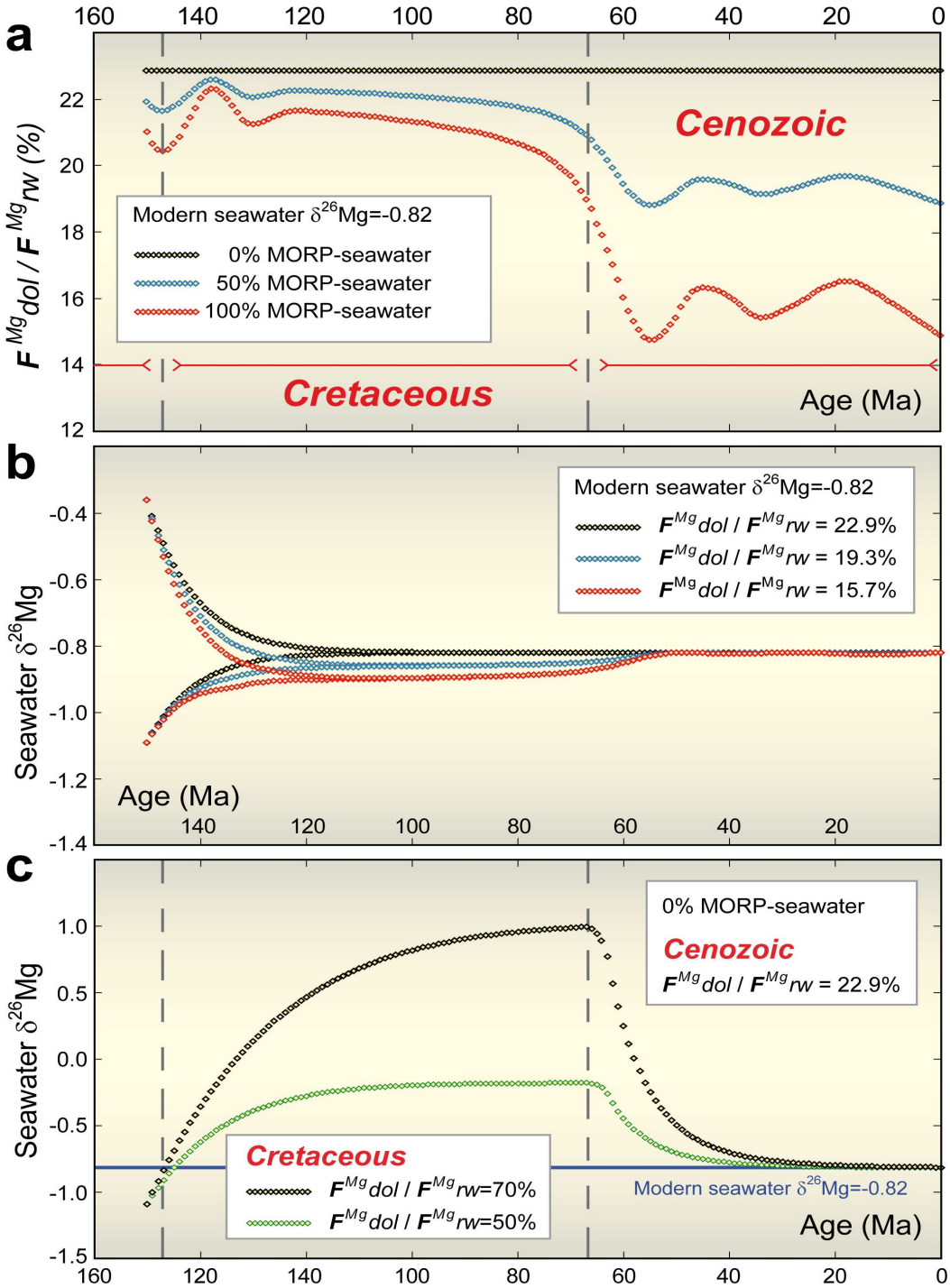

Figure S11. *Mg-removal constraints from Mg isotope ratio.* ***a,*** *temporal variations of Mg-removal flux due to dolomite deposition inferred at different volumes of mantle that can interact yearly with seawater at T < 150 °C, assuming steady state seawater Mg isotopic composition.* ***b,*** *temporal changes of seawater* δ^{26}*Mg due to Mg-release by MORP-seawater reactions for different volumes of mantle that can interact yearly with seawater at T < 150 °C and for different initial conditions, assuming a constant flux of dolomite Mg-removal, obtained iteratively to fit the modern ocean* δ^{26}*Mg of seawater.* ***c,*** *variations of seawater* δ^{26}*Mg, assuming no Mg contribution from MORP-seawater reactions and assuming a greater Mg-removal flux due to dolomite deposition during the Cretaceous than that during the Cenozoic.*

Table S1. *Volume (m^3/yr) of mantle rocks ($Vol_{<150°C}$) that can interact yearly with seawater at T < 150 °C estimated at each segment of the global mid-ocean ridge system. Latitude (Lat), Longitude (Long), half spreading rate (V_s) and spreading direction (a_s) are referred to the mid-point of each ridge segment (#). Spreading rates (mm/yr) and directions (azimuth, degree) were obtained using MORVEL angular velocities (ref. 3). L_{seg}, L_{off}^1 and L_{off}^2 are the lengths (km) of the ridge segment and of the two bounding transform offsets. H_c is the mean crustal thickness (km) at ridge segment. Plate name abbreviations are as follows: AN, Antarctic; AR, Arabia; AU, Australia; CO, Cocos; CP, Capricorn; EU, Eurasia; IN, India; JF, Juan de Fuca; LW, Lwandle; NA, North America; NB, Nubia; NZ, Nazca; PA, Pacific; SA, South America; SM, Somalia and SR, Sur. Mg_{rel} is the amount of Mg that can be released yearly to seawater from hydration of the oceanic mantle.*

South West Indian Ridge (SWIR)

Plate	Ridge	#	Lat	Long	V_s	α_s	L_{seg}	L_{off}^1	L_{off}^2	H_c	$Vol_{<150℃}$
SM-AN	SWIR	1	-26.56300	67.81948	6.30	354.67	423.48	0.00	29.67	1.56	7588975
SM-AN	SWIR	2	-27.53997	65.82392	6.44	355.02	97.36	29.67	30.66	1.53	2057335
SM-AN	SWIR	3	-27.97186	63.90687	6.57	355.72	253.20	30.66	28.04	1.67	4379756
SM-AN	SWIR	4	-28.40468	62.48292	6.66	356.19	65.05	28.04	45.89	1.47	1620009
SM-AN	SWIR	5	-28.81275	61.80463	6.70	356.29	65.39	45.89	21.63	1.50	1554555
SM-AN	SWIR	6	-28.99793	61.10407	6.74	356.55	64.16	21.63	137.44	1.22	2200814
SM-AN	SWIR	7	-30.66291	59.64672	6.84	356.40	254.88	137.44	50.27	1.50	5610136
SM-AN	SWIR	8	-31.70996	57.68906	6.94	356.92	131.11	50.27	203.61	1.12	4272373
SM-AN	SWIR	9	-33.70055	56.39605	7.02	356.68	131.24	203.61	66.66	1.08	4417996
SM-AN	SWIR	10	-34.36110	55.24813	7.07	357.05	60.32	66.66	44.39	1.31	1866287
SM-AN	SWIR	11	-34.74418	54.48724	7.11	357.32	66.74	44.39	62.28	1.35	1925342
SM-AN	SWIR	12	-35.34749	53.87608	7.14	357.42	44.61	62.28	0.00	1.42	1233203
LW-AN	SWIR	1	-35.44980	53.52162	7.37	0.70	21.06	0.00	76.02	1.38	762988
LW-AN	SWIR	2	-36.12830	52.85346	7.36	1.13	92.58	76.02	111.63	1.13	3110012
LW-AN	SWIR	3	-38.00976	49.14486	7.33	3.56	576.51	111.63	141.94	1.94	7795241
LW-AN	SWIR	4	-40.30028	45.34907	7.29	6.32	138.86	141.94	40.96	1.47	3436059
LW-AN	SWIR	5	-40.98222	43.60392	7.26	7.61	143.34	40.96	217.88	1.32	4078443
LW-AN	SWIR	6	-42.79260	42.11284	7.25	8.99	47.69	217.88	130.99	0.57	2832534
LW-AN	SWIR	7	-43.89076	40.90934	7.23	10.08	91.79	130.99	47.86	1.19	2912442
LW-AN	SWIR	8	-43.39413	39.84900	7.21	10.74	84.44	47.86	101.01	1.23	2648334
LW-AN	SWIR	9	-44.52763	37.40200	7.16	12.80	324.31	101.01	175.19	1.62	6629348
LW-AN	SWIR	10	-46.10050	34.31334	7.11	15.57	71.35	175.19	147.81	0.66	3551620
LW-AN	SWIR	11	-47.20813	32.93099	7.09	16.97	76.67	147.81	105.44	0.80	3362003
LW-AN	SWIR	12	-48.04974	31.81229	7.07	18.12	23.48	105.44	133.23	0.73	1462203
LW-AN	SWIR	13	-49.13129	30.54540	7.05	19.48	21.04	133.23	0.00	0.94	1128966
NB-AN	SWIR	1	-49.18814	30.35341	8.20	15.76	10.22	0.00	456.57	0.84	1142165
NB-AN	SWIR	2	-52.67615	26.74986	8.14	20.18	137.95	456.57	137.41	0.97	5787635
NB-AN	SWIR	3	-52.76229	18.76308	7.87	27.50	1012.67	137.41	31.24	2.43	3958578
NB-AN	SWIR	4	-52.94640	10.13585	7.55	36.00	32.17	31.24	199.15	1.33	1491546
NB-AN	SWIR	5	-54.10965	7.81689	7.52	38.95	32.01	199.15	23.08	1.39	1431316
NB-AN	SWIR	6	-53.98690	7.01534	7.48	39.72	60.34	23.08	119.37	1.52	1753867
NB-AN	SWIR	7	-54.45521	5.12765	7.44	41.94	57.80	119.37	22.70	1.47	1694503
NB-AN	SWIR	8	-54.05075	3.84523	7.37	43.11	120.48	22.70	222.66	1.43	3359277
NB-AN	SWIR	9	-54.89757	0.30274	7.30	47.37	57.59	222.66	28.64	1.20	2271104
NB-AN	SWIR	10	-54.87546	-0.55455	7.27	48.31	28.47	28.64	0.00	2.22	408448

SWIR – $Vol_{<150℃}$ = 105.735·10^6 m^3/yr – Mg_{rel} = 4.368 10^{11} mol/yr

Vol_{MORB} = 118.697·10^6 m^3/yr

Mid Atlantic Ridge (MAR)

Plate	Ridge	#	Lat	Long	V_s	α_s	L_{seg}	L_{off}^1	L_{off}^2	H_c	$Vol_{<150℃}$
NB-SA	MAR	1	-54.42046	-1.15217	14.37	70.60	102.38	0.00	68.34	5.42	13068
NB-SA	MAR	2	-53.75606	-2.91932	14.50	71.61	124.81	68.34	43.29	5.19	11280
NB-SA	MAR	3	-52.84727	-4.35382	14.65	72.48	133.93	43.29	36.71	5.54	0
NB-SA	MAR	4	-51.43018	-5.92756	14.86	73.46	240.66	36.71	27.88	5.85	0
NB-SA	MAR	5	-50.31319	-7.08888	15.01	74.17	47.57	27.88	42.64	5.49	0
NB-SA	MAR	6	-49.66685	-8.04556	15.10	74.72	154.94	42.64	113.21	5.20	239180
NB-SA	MAR	7	-48.96331	-10.05508	15.22	75.78	96.47	113.21	32.50	4.95	221435
NB-SA	MAR	8	-47.75196	-10.21190	15.34	75.97	169.25	32.50	220.77	5.04	723840
NB-SA	MAR	9	-44.39444	-15.22841	15.72	78.63	909.74	220.77	41.86	5.99	765631
NB-SA	MAR	10	-40.16951	-16.47580	16.04	79.41	50.48	41.86	59.56	5.29	0
NB-SA	MAR	11	-39.00470	-16.07861	16.10	79.26	168.56	59.56	61.61	5.76	0
NB-SA	MAR	12	-37.22709	-17.43766	16.20	79.94	336.28	61.61	255.44	5.65	966922
NB-SA	MAR	13	-34.81615	-15.11404	16.29	78.90	109.59	255.44	64.35	4.28	870357
NB-SA	MAR	14	-33.94673	-14.52949	16.31	78.65	57.54	64.35	24.52	5.49	0
NB-SA	MAR	15	-33.04515	-14.44955	16.34	78.63	131.65	24.52	127.40	5.43	209531
NB-SA	MAR	16	-31.77377	-13.38542	16.37	78.15	88.03	127.40	17.71	5.26	202467
NB-SA	MAR	17	-31.02849	-13.41104	16.38	78.17	72.04	17.71	16.35	6.44	0
NB-SA	MAR	18	-30.28986	-13.75735	16.40	78.33	99.97	16.35	23.37	6.25	0
NB-SA	MAR	19	-29.55987	-13.67483	16.41	78.30	54.05	23.37	66.80	5.62	0
NB-SA	MAR	20	-29.10059	-13.08102	16.41	78.03	23.11	66.80	64.91	4.48	0
NB-SA	MAR	21	-28.54113	-12.53931	16.42	77.79	78.59	64.91	58.10	5.31	0
NB-SA	MAR	22	-26.79566	-13.63495	16.43	78.27	290.44	58.10	40.99	6.12	0
NB-SA	MAR	23	-25.33835	-13.64005	16.42	78.25	81.07	40.99	51.08	5.72	0
NB-SA	MAR	24	-23.90301	-13.44429	16.41	78.14	213.53	51.08	89.77	5.80	69083
NB-SA	MAR	25	-22.59673	-12.82059	16.39	77.84	43.02	89.77	122.21	3.46	269853
NB-SA	MAR	26	-21.74893	-11.79814	16.37	77.37	97.73	122.21	36.05	5.09	191386
NB-SA	MAR	27	-19.62899	-11.99782	16.31	77.39	313.26	36.05	48.85	6.12	0
NB-SA	MAR	28	-18.15743	-12.85481	16.25	77.72	104.41	48.85	125.34	5.07	210114
NB-SA	MAR	29	-17.15771	-14.24255	16.20	78.29	168.00	125.34	127.42	5.03	457775
NB-SA	MAR	30	-15.09301	-13.44096	16.10	77.84	245.12	127.42	84.07	5.53	279506
NB-SA	MAR	31	-13.26224	-14.63173	15.98	78.28	205.97	84.07	58.13	5.65	46255
NB-SA	MAR	32	-12.02489	-14.34959	15.89	78.08	44.63	58.13	163.90	3.75	347901
NB-SA	MAR	33	-9.35053	-13.21921	15.71	77.38	491.75	163.90	257.06	5.59	1505655
NB-SA	MAR	34	-5.82992	-11.41381	15.44	76.28	191.45	257.06	82.12	4.75	1083945
NB-SA	MAR	35	-4.85405	-12.36786	15.32	76.61	64.06	82.12	23.53	5.15	53411
NB-SA	MAR	36	-4.24617	-12.27880	15.26	76.51	54.91	23.53	29.03	5.94	0
NB-SA	MAR	37	-3.48483	-12.16008	15.18	76.38	101.12	29.03	21.59	5.96	0
NB-SA	MAR	38	-2.60188	-12.12997	15.09	76.27	83.68	21.59	47.78	5.63	0
NB-SA	MAR	39	-2.17380	-12.65075	15.03	76.47	30.77	47.78	21.84	5.53	0
NB-SA	MAR	40	-1.46389	-12.99495	14.94	76.55	137.74	21.84	317.60	4.43	1351719
NB-SA	MAR	41	-0.28708	-16.44551	14.70	78.06	247.82	317.60	868.94	3.73	5463107
NB-SA	MAR	42	-0.25523	-24.77940	14.51	82.29	208.57	868.94	56.72	4.12	3241942
NB-SA	MAR	43	0.71029	-25.46979	14.37	82.58	21.82	56.72	96.81	3.30	186082
NB-SA	MAR	44	0.84224	-26.36207	14.34	83.04	26.27	96.81	144.67	2.42	691102
NB-SA	MAR	45	0.99269	-27.67949	14.29	83.74	34.62	144.67	302.85	1.56	1930624
NB-SA	MAR	46	1.53091	-30.55879	14.18	85.28	206.43	302.85	58.64	4.50	1551787
NB-SA	MAR	47	3.32994	-31.42555	13.90	85.66	156.84	58.64	116.46	4.63	373508
NB-SA	MAR	48	5.25665	-32.89355	13.59	86.40	279.63	116.46	51.20	4.98	417673

NB-SA	MAR	49	6.73919	-33.82498	13.33	86.88	103.93	51.20	82.49	4.31	153660
NB-SA	MAR	50	7.32260	-34.62577	13.23	87.33	29.81	82.49	231.45	1.97	1131812
NB-SA	MAR	51	7.59660	-36.73218	13.17	88.58	40.23	231.45	144.51	1.65	1798516
NB-SA	MAR	52	8.00049	-38.04350	13.10	89.37	53.12	144.51	175.19	1.98	1464363
NB-SA	MAR	53	8.53715	-39.56299	13.00	90.29	80.02	175.19	111.88	2.64	1315939
NB-SA	MAR	54	9.79728	-40.69540	12.78	90.99	227.59	111.88	308.81	3.79	2416215
NB-SA	MAR	55	11.57014	-43.71950	12.48	92.93	139.50	308.81	43.19	3.44	1667667
NB-SA	MAR	56	12.46826	-44.10813	12.31	93.21	53.37	43.19	82.38	3.50	214794
NB-SA	MAR	57	13.41714	-44.91900	12.14	93.78	134.47	82.38	0.00	4.63	235322
NB-SA	MAR	58	14.59160	-45.03293	12.51	101.00	153.06	0.00	176.09	4,77	775863
NB-NA	MAR	1	17.13520	-46.58871	12.37	101.13	363.81	176.09	32.71	4,99	894714
NB-NA	MAR	2	20.66722	-45.61224	12.10	101.36	608.23	32.71	149.90	4.66	804304
NB-NA	MAR	3	27.14688	-44.40225	11.49	101.93	801.72	149.90	68.14	4.43	1093138
NB-NA	MAR	4	32.10404	-40.36126	10.86	102.52	511.05	68.14	116.53	4.01	1071302
NB-NA	MAR	5	33.82348	-37.71918	10.58	102.74	67.55	116.53	42.57	2.62	741613
NB-NA	MAR	6	34.30373	-37.11296	10.50	102.80	55.89	42.57	47.75	3.30	89378
NB-NA	MAR	7	34.88505	-36.42242	10.41	102.88	91.82	47.75	129.02	2.65	945285
NB-NA	MAR	8	35.35090	-34.84295	10.31	102.92	65.99	129.02	46.45	2.37	907728
NB-NA	MAR	9	35.88385	-34.15591	10.22	102.99	71.65	46.45	26.03	3.57	63805
NB-NA	MAR	10	36.36878	-33.70025	10.14	103.06	51.78	26.03	28.21	3.82	0
NB-NA	MAR	11	36.74436	-33.24985	10.08	103.12	43.93	28.21	20.65	3.81	0
NB-NA	MAR	12	37.03790	-32.90330	10.03	103.16	28.36	20.65	43.53	3.63	44787
NB-NA	MAR	13	37.31200	-32.29036	9.97	103.19	52.81	43.53	39.91	3.25	83445
NB-NA	MAR	14	37.76353	-31.64726	9.89	103.25	69.45	39.91	51.36	3.10	187992
NB-NA	MAR	15	38.61590	-30.55647	9.74	103.37	170.56	51.36	0.00	3.65	176498
EU-NA	MAR	1	39.79398	-29.81542	11.45	94.80	157.24	0.00	20.22	4.79	0
EU-NA	MAR	2	42.19823	-29.22819	11.34	95.11	366.42	20.22	32.47	4.49	0
EU-NA	MAR	3	48.41131	-28.29348	10.96	95.71	1014.47	32.47	118.50	4.24	827852
EU-NA	MAR	4	52.36942	-31.69022	10.67	94.10	43.46	118.50	238.36	1.11	2365105
EU-NA	MAR	5	54.15633	-35.16262	10.53	92.33	361.61	238.36	29.79	3.67	1709391
EU-NA	MAR	6	56.32569	-34.37242	10.32	92.78	104.79	29.79	21.91	4.01	0
EU-NA	MAR	7	61.62703	-26.49346	9.73	97.35	1033.79	21.91	14.80	3.73	0
EU-NA	MAR	8	63.95557	-22.01914	9.42	100.13	17.57	14.80	21.15	3.63	0
EU-NA	MAR	9	64.11016	-21.27417	9.39	100.58	44.14	21.15	13.38	3.60	0
EU-NA	MAR	10	66.76140	-18.56259	9.04	102.58	564.62	13.38	46.82	3.24	269331
EU-NA	MAR	11	69.76465	-15.59174	8.61	105.01	234.09	46.82	79.00	2.60	1373897
EU-NA	MAR	12	70.82870	-12.13916	8.42	107.48	75.42	79.00	33.40	2.10	1150079
EU-NA	MAR	13	71.49955	-12.15445	8.33	107.66	56.56	33.40	211.96	1.60	1942153
EU-NA	MAR	14	74.22753	3.39232	7.68	119.26	1145.89	211.96	115.48	2.27	8152818
EU-NA	MAR	15	79.38061	3.73041	6.98	122.68	61.13	115.48	0.00	0.96	2302364

MAR – $Vol_{<150℃}$ = 62.317 10^6 m^3/yr – Mg_{rel} = 2.574 10^{11} mol/yr

Vol_{MORB} = 1971.477·10^6 m^3/yr

Gakkel Ridge

Plate	Ridge	#	Lat	Long	V_s	α_s	L_{seg}	L_{off}^1	L_{off}^2	H_c	$Vol_{<150℃}$
EU-NA	Gakkel	1	79.43151	3.28810	6.98	122.37	67.63	0.00	145.47	1.37	2025431
EU-NA	Gakkel	2	80.79494	-2.62758	6.87	118.53	93.24	145.47	39.89	1.16	3036492
EU-NA	Gakkel	3	81.68984	-4.52123	6.77	117.52	68.43	39.89	24.99	1.62	1514627
EU-NA	Gakkel	4	83.29477	-3.40629	6.52	119.39	308.16	24.99	16.63	1.68	5185889
EU-NA	Gakkel	5	85.47513	16.89902	6.02	139.43	313.95	16.63	5.39	1.40	6227209
EU-NA	Gakkel	6	86.25888	36.05575	5.74	159.04	76.73	5.39	10.05	1.25	1746717
EU-NA	Gakkel	7	86.82696	53.26358	5.53	177.63	156.44	10.05	13.27	1.10	3676189
EU-NA	Gakkel	8	85.94420	79.29794	5.22	203.47	345.66	13.27	15.63	0.90	8407434
EU-NA	Gakkel	9	84.31285	107.15284	4.69	231.73	249.78	15.63	11.29	0.68	6776712
EU-NA	Gakkel	10	80.64899	121.78009	3.91	244.93	699.87	11.29	0.00	0.46	20466647

Gakkel – $Vol_{<150℃}$ = 59.063 10^6 m^3/yr – Mg_{rel} = 2.440 10^{11} mol/yr

Vol_{MORB} = 26.674·10^6 m^3/yr

America-Antarctica Ridge (AAR)

Plate	Ridge	#	Lat	Long	V_s	α_s	L_{seg}	L_{off}^1	L_{off}^2	H_c	$Vol_{<150℃}$
AN-SR	AAR	1	-60.94715	-25.39575	8.19	81.90	3.98	0.00	328.04	1.82	465292
AN-SR	AAR	2	-60.56702	-19.39065	8.18	82.31	49.95	328.04	36.70	1.22	2380848
AN-SR	AAR	3	-60.12878	-18.77146	8.29	82.47	41.21	36.70	17.47	2.56	304009
AN-SR	AAR	4	-59.55641	-18.27576	8.43	82.64	94.52	17.47	93.12	2.21	1144690
AN-SR	AAR	5	-58.81533	-16.17409	8.59	82.96	77.30	93.12	529.70	0.79	4390669
AN-SR	AAR	6	-57.33715	-6.56108	8.82	84.03	161.01	529.70	49.27	1.74	4146666
AN-SR	AAR	7	-56.56627	-5.39924	9.00	84.28	19.48	49.27	47.48	2.24	480909
AN-SR	AAR	8	-56.14598	-4.72383	9.10	84.41	51.17	47.48	201.72	1.61	1810675
AN-SR	AAR	9	-55.37539	-1.51221	9.26	84.84	72.43	201.72	30.87	2.13	1408395
AN-SR	AAR	10	-54.92769	-0.77331	9.36	84.98	25.04	30.87	0.00	3.60	3731

AAR – $Vol_{<150℃}$ = 16.536 10^6 m^3/yr – Mg_{rel} = 0.683 10^{11} mol/yr

Vol_{MORB} = 18.825·10^6 m^3/yr

Central Indian Ridge (CIR)

Plate	Ridge	#	Lat	Long	V_s	α_s	L_{seg}	L_{off}^1	L_{off}^2	H_c	$Vol_{<150℃}$
CP-SM	CIR	1	-25.39754	69.95594	23.70	58.84	28.02	0.00	28.41	8.11	0
CP-SM	CIR	2	-24.91914	69.93925	23.55	58.63	55.39	28.41	13.43	7.40	0
CP-SM	CIR	3	-24.49692	69.77563	23.38	58.60	35.82	13.43	15.25	7.56	0
CP-SM	CIR	4	-24.03367	69.62511	23.21	58.54	60.27	15.25	11.05	7.75	0
CP-SM	CIR	5	-23.45986	69.32949	22.97	58.58	74.27	11.05	19.16	7.63	0
CP-SM	CIR	6	-22.97274	69.19277	22.78	58.49	30.27	19.16	36.74	7.35	0
CP-SM	CIR	7	-22.43560	69.23200	22.61	58.16	58.23	36.74	20.61	7.23	0
CP-SM	CIR	8	-21.62753	68.89567	22.28	58.11	122.02	20.61	24.38	7.32	0
CP-SM	CIR	9	-20.89540	68.66261	21.99	57.97	32.01	24.38	18.45	7.53	0
CP-SM	CIR	10	-20.56164	68.22561	21.79	58.29	71.68	18.45	32.37	7.06	0
CP-SM	CIR	11	-20.25139	67.64467	21.57	58.81	46.41	32.37	66.48	6.47	0
CP-SM	CIR	12	-20.20627	66.85359	21.40	59.74	50.38	66.48	42.79	6.36	0
CP-SM	CIR	13	-18.98482	65.63217	20.72	60.56	282.20	42.79	213.80	6.65	349246
CP-SM	CIR	14	-16.77081	66.67433	20.13	57.86	59.32	213.80	106.32	3.99	372076

CP-SM	CIR	15	-15.82979	67.24255	19.92	56.51	61.47	106.32	20.73	5.85	6256
CP-SM	CIR	16	-15.12889	67.00343	19.61	56.31	92.38	20.73	21.57	6.99	0
CP-SM	CIR	17	-14.47151	66.26349	19.20	56.79	136.16	21.57	106.16	6.33	35258
CP-SM	CIR	18	-12.68273	66.12654	18.50	55.60	185.18	106.16	106.71	5.86	135977
CP-SM	CIR	19	-11.37086	66.26886	18.05	54.33	49.38	106.71	70.40	4.47	86728
CP-SM	CIR	20	-10.57452	66.46904	17.81	53.37	75.01	70.40	79.38	5.24	0
CP-SM	CIR	21	-9.76353	66.73598	17.59	52.28	32.09	79.38	236.34	3.23	560338
CP-SM	CIR	22	-8.15604	68.15918	17.42	48.87	26.85	236.34	0.00	3.23	529136
IN-SM	CIR	1	-7.94329	67.96945	16.74	41.04	34.75	0.00	58.61	4.74	0
IN-SM	CIR	2	-7.28876	68.09257	16.65	40.50	50.85	58.61	88.52	4.60	47066
IN-SM	CIR	3	-6.30581	68.27944	16.52	39.66	78.03	88.52	113.45	4.36	223491
IN-SM	CIR	4	-5.11676	68.57101	16.37	38.57	58.07	113.45	59.97	4.41	166593
IN-SM	CIR	5	-4.32002	68.54089	16.23	37.98	68.89	59.97	60.82	5.16	0
IN-SM	CIR	6	-3.45216	68.34445	16.04	37.43	89.55	60.82	39.90	5.52	0
IN-SM	CIR	7	-2.77722	68.09861	15.87	37.05	45.62	39.90	56.84	5.15	0
IN-SM	CIR	8	-2.09492	68.14921	15.77	36.45	47.69	56.84	14.10	5.52	0
IN-SM	CIR	9	-1.60709	67.74031	15.59	36.31	94.59	14.10	46.43	5.94	0
IN-SM	CIR	10	-0.85526	67.48326	15.40	35.82	48.38	46.43	5.64	5.89	0
IN-SM	CIR	11	-0.51374	67.18074	15.27	35.71	50.27	5.64	32.40	6.16	0
IN-SM	CIR	12	-0.07540	67.13848	15.19	35.34	19.21	32.40	15.60	6.10	0
IN-SM	CIR	13	0.20910	67.04647	15.12	35.14	34.66	15.60	57.66	5.42	0
IN-SM	CIR	14	1.89359	66.62253	14.73	33.81	373.54	57.66	24.61	5.76	0
IN-SM	CIR	15	4.13190	63.22371	13.48	33.64	513.98	24.61	24.67	5.36	0
IN-SM	CIR	16	6.47085	60.53465	12.34	32.66	306.93	24.67	39.07	4.89	0
IN-SM	CIR	17	7.86188	59.40582	11.78	31.58	83.33	39.07	18.35	4.49	0
IN-SM	CIR	18	8.21730	58.66702	11.50	31.61	89.18	18.35	29.57	4.52	0
IN-SM	CIR	19	8.79347	58.36177	11.31	30.98	30.34	29.57	28.02	4.45	0
IN-SM	CIR	20	9.22969	58.20477	11.19	30.44	48.77	28.02	23.92	4.35	0
IN-SM	CIR	21	9.78743	57.83138	10.98	29.84	84.32	23.92	42.52	4.10	7199
IN-SM	CIR	22	9.90313	57.02568	10.73	30.24	65.26	42.52	334.55	2.07	1710490
IN-SM	CIR	23	12.89092	57.86974	10.50	24.68	114.29	334.55	56.52	2.24	2285364
IN-SM	CIR	24	13.67325	57.45661	10.26	23.51	39.84	56.52	0.00	3.54	124910
AR-SM	CIR	1	13.81641	57.14068	12.00	21.59	42.33	0.00	19.99	5.27	0
AR-SM	CIR	2	14.57111	55.36390	11.32	21.01	353.35	19.99	48.06	4.43	30707
AR-SM	CIR	3	14.37428	53.57943	10.76	22.12	46.21	48.06	14.03	3.88	47944
AR-SM	CIR	4	14.53199	52.75063	10.46	22.23	129.69	14.03	203.60	3.05	1257564
AR-SM	CIR	5	13.26078	50.44581	9.89	26.06	176.96	203.60	90.16	2.53	2419251
AR-SM	CIR	6	12.90230	49.04541	9.50	27.85	47.95	90.16	39.88	2.22	760742
AR-SM	CIR	7	12.76490	48.57189	9.37	28.53	20.87	39.88	26.96	3.24	65906
AR-SM	CIR	8	12.69043	48.22177	9.27	28.99	29.60	26.96	43.67	2.95	124884
AR-SM	CIR	9	12.52322	47.72229	9.13	29.80	36.90	43.67	44.55	2.57	396311
AR-SM	CIR	10	12.36640	47.18097	8.99	30.66	36.66	44.55	37.05	2.65	335930
AR-SM	CIR	11	12.25244	46.71483	8.86	31.38	29.23	37.05	32.80	2.79	190156
AR-SM	CIR	12	12.15333	46.29018	8.75	32.05	33.93	32.80	34.01	2.73	184092
AR-SM	CIR	13	11.89461	44.10414	8.11	35.28	385.82	34.01	0.00	2.72	280671

CIR – $Vol_{<150℃}$ = 12.734 10^6 m^3/yr – Mg_{rel} = 0.526 10^{11} mol/yr

Vol_{MORB} = 878.091·10^6 m^3/yr

Pacific Ridge (PAC)

Plate	Ridge	#	Lat	Long	V_s	α_s	L_{seg}	L_{off}^1	L_{off}^2	H_c	$Vol_{<150℃}$
PA-AN	PAC	1	-65.71152	-176.17723	25.96	320.44	66.38	0.00	23.18	8.10	0
PA-AN	PAC	2	-65.32982	-174.39261	26.54	319.04	110.29	23.18	18.48	7.84	0
PA-AN	PAC	3	-64.94025	-172.73328	27.10	317.74	58.52	18.48	11.86	8.12	0
PA-AN	PAC	4	-64.48459	-171.84381	27.51	316.79	71.41	11.86	63.16	7.61	0
PA-AN	PAC	5	-64.09029	-168.98540	28.32	314.95	187.03	63.16	25.35	7.77	0
PA-AN	PAC	6	-63.12367	-166.12994	29.40	312.64	164.11	25.35	31.12	7.94	0
PA-AN	PAC	7	-62.66352	-164.31827	30.00	311.37	28.32	31.12	32.50	8.07	0
PA-AN	PAC	8	-62.48879	-163.07388	30.34	310.63	80.36	32.50	143.25	7.22	0
PA-AN	PAC	9	-62.76181	-159.78205	30.86	309.27	88.78	143.25	107.07	6.83	0
PA-AN	PAC	10	-62.57845	-156.65853	31.55	307.62	131.31	107.07	44.11	7.65	0
PA-AN	PAC	11	-60.90984	-153.20418	33.01	304.86	380.20	44.11	62.85	8.04	0
PA-AN	PAC	12	-58.61238	-149.17188	34.85	301.74	279.24	62.85	69.46	8.03	0
PA-AN	PAC	13	-56.71515	-145.99896	36.29	299.47	260.22	69.46	365.63	7.58	684941
PA-AN	PAC	14	-55.65545	-138.40946	37.92	295.79	378.24	365.63	137.84	7.85	656480
PA-AN	PAC	15	-54.23161	-134.82312	39.04	293.79	100.42	137.84	467.76	5.95	1042353
PA-AN	PAC	16	-55.10536	-127.60113	39.49	290.84	67.77	467.76	392.87	3.68	1809879
PA-AN	PAC	17	-55.08546	-121.10869	40.14	287.88	214.46	392.87	145.53	7.34	706205
PA-AN	PAC	18	-53.82074	-118.09523	40.96	286.28	171.29	145.53	55.10	7.83	0
PA-AN	PAC	19	-51.11759	-117.58648	42.12	285.65	424.67	55.10	211.31	8.08	0
PA-AN	PAC	20	-46.13295	-112.70575	44.28	283.03	986.97	211.31	41.91	8.21	0
PA-AN	PAC	21	-37.92818	-111.04275	46.64	281.90	671.09	41.91	0.00	7.83	0
NZ-PA	PAC	1	-34.28819	-112.22581	73.86	105.36	277.11	0.00	21.68	7.72	0
NZ-PA	PAC	2	-32.84735	-112.44971	73.81	105.42	176.70	21.68	25.79	7.96	0
NZ-PA	PAC	3	-31.89950	-112.06938	73.75	105.17	108.94	25.79	1.16	8.33	0
NZ-PA	PAC	4	-30.11050	-111.80682	73.59	104.96	293.85	1.16	87.59	8.32	0
NZ-PA	PAC	5	-28.64602	-112.98379	73.44	105.58	294.13	87.59	0.87	8.38	0
NZ-PA	PAC	6	-25.81924	-115.50433	73.09	106.94	428.42	0.87	107.27	8.43	0
NZ-PA	PAC	7	-23.79812	-115.47167	72.69	106.92	68.27	107.27	60.64	7.94	0
NZ-PA	PAC	8	-23.20816	-115.05990	72.54	106.70	19.34	60.64	47.49	7.73	0
NZ-PA	PAC	9	-22.86185	-114.57168	72.42	106.43	36.84	47.49	1.95	8.47	0
NZ-PA	PAC	10	-18.02756	-113.45808	70.92	105.90	1063.09	1.95	141.36	8.47	0
NZ-PA	PAC	11	-11.16815	-110.50307	67.70	104.53	535.54	141.36	178.23	8.28	0
NZ-PA	PAC	12	-7.76924	-107.89435	65.54	103.18	325.48	178.23	66.31	8.09	0
NZ-PA	PAC	13	-5.42506	-106.60367	63.96	102.56	237.25	66.31	176.98	8.03	0
NZ-PA	PAC	14	-4.09413	-104.56710	62.83	101.34	128.67	176.98	192.72	7.68	0
NZ-PA	PAC	15	-1.27016	-102.41788	60.59	100.12	552.58	192.72	2.55	8.50	0
NZ-PA	PAC	16	1.88292	-102.24950	58.20	100.32	156.19	2.55	0.00	8.85	0
CO-PA	PAC	1	4.44065	-102.31898	61.71	79.74	638.06	0.00	142.37	8.57	0
CO-PA	PAC	2	9.27987	-104.21972	53.24	81.17	191.38	142.37	75.74	8.00	0
CO-PA	PAC	3	12.94955	-104.03582	46.99	79.61	572.22	75.74	93.49	8.30	0
CO-PA	PAC	4	15.70090	-105.40924	41.76	81.23	115.60	93.49	13.29	8.04	0
CO-PA	PAC	5	17.57230	-105.46856	38.39	80.61	275.81	13.29	412.57	7.72	813656
CO-PA	PAC	6	21.44794	-108.64427	30.69	87.49	345.12	412.57	84.83	7.60	1019038
CO-PA	PAC	7	23.44527	-108.54756	26.95	86.88	52.53	84.83	58.05	6.71	0
CO-PA	PAC	8	24.01862	-108.85333	25.84	87.81	20.12	58.05	56.04	6.85	0
CO-PA	PAC	9	24.55885	-109.14306	24.81	88.76	35.82	56.04	115.05	5.62	0
CO-PA	PAC	10	25.44207	-109.86998	23.14	91.48	37.13	115.05	132.73	4.55	1957
CO-PA	PAC	11	26.34764	-110.77030	21.51	95.33	16.57	132.73	97.66	4.34	36748
CO-PA	PAC	12	27.02547	-111.42730	20.37	98.52	21.09	97.66	43.06	5.31	0

CO-PA	PAC	13	27.46965	-111.60739	19.58	99.71	36.10	43.06	332.04	3.82	841998
CO-PA	PAC	14	29.78002	-113.87735	16.45	114.52	36.69	332.04	0.00	1.57	1712956
JF-PA	PAC	1	40.36701	-124.73290	23.66	115.60	12.15	0.00	229.22	3.03	476660
JF-PA	PAC	2	41.03483	-127.44211	23.56	111.49	126.88	229.22	17.00	6.44	341627
JF-PA	PAC	3	41.99473	-127.12224	24.00	111.53	84.72	17.00	14.87	7.67	0
JF-PA	PAC	4	42.68222	-126.75112	24.32	111.75	70.83	14.87	190.41	6.20	154841
JF-PA	PAC	5	43.75940	-128.72448	24.54	108.61	18.62	190.41	158.14	3.82	206844
JF-PA	PAC	6	46.70311	-129.43651	25.66	106.66	526.83	158.14	137.13	7.58	14695
JF-PA	PAC	7	50.07888	-130.08947	26.91	104.84	177.73	137.13	0.00	7.43	0

PAC – $Vol_{<150℃}$ = 10.520 10^6 m^3/yr – Mg_{rel} = 0.435 10^{11} mol/yr

Vol_{MORB} = 11589.773·10^6 m^3/yr

Nazca Ridge

Plate	*Ridge*	*#*	*Lat*	*Long*	V_s	α_s	L_{seg}	L_{off}^1	L_{off}^2	H_c	$Vol_{<150℃}$
NZ-AN	NAZCA	1	-45.95902	-75.92353	26.27	73.62	36.79	0.00	59.25	7.67	0
NZ-AN	NAZCA	2	-45.78001	-76.81061	26.25	74.34	38.17	59.25	78.72	6.55	0
NZ-AN	NAZCA	3	-45.10275	-78.11847	26.18	75.38	155.01	78.72	291.02	6.45	412498
NZ-AN	NAZCA	4	-44.12948	-82.28358	26.03	78.78	236.10	291.02	60.96	7.00	426234
NZ-AN	NAZCA	5	-42.48965	-83.58122	25.85	79.77	124.53	60.96	20.70	7.53	0
NZ-AN	NAZCA	6	-41.85966	-83.98133	25.77	80.06	23.21	20.70	20.01	7.86	0
NZ-AN	NAZCA	7	-41.67624	-84.27791	25.75	80.30	22.97	20.01	28.75	7.77	0
NZ-AN	NAZCA	8	-41.53589	-84.68089	25.73	80.63	18.44	28.75	74.83	7.04	0
NZ-AN	NAZCA	9	-41.42657	-85.64753	25.70	81.45	26.34	74.83	172.98	5.13	0
NZ-AN	NAZCA	10	-41.41703	-87.76043	25.67	83.26	22.99	172.98	117.22	4.43	0
NZ-AN	NAZCA	11	-41.32419	-89.17822	25.65	84.48	16.73	117.22	97.15	5.20	0
NZ-AN	NAZCA	12	-41.26012	-90.34585	25.63	85.48	14.89	97.15	76.40	5.72	0
NZ-AN	NAZCA	13	-41.15974	-91.26639	25.61	86.27	15.41	76.40	52.66	6.23	0
NZ-AN	NAZCA	14	-40.66945	-91.91550	25.54	86.81	90.12	52.66	27.77	7.43	0
NZ-AN	NAZCA	15	-39.73436	-91.59370	25.42	86.49	147.18	27.77	88.40	7.24	0
NZ-AN	NAZCA	16	-38.67273	-92.60607	25.26	87.33	67.91	88.40	109.33	5.95	0
NZ-AN	NAZCA	17	-38.25016	-93.86899	25.19	88.42	25.27	109.33	18.17	6.38	0
NZ-AN	NAZCA	18	-37.71169	-94.09828	25.11	88.61	94.68	18.17	111.00	7.00	0
NZ-AN	NAZCA	19	-37.18676	-95.36135	25.03	89.71	22.10	111.00	150.50	4.76	0
NZ-AN	NAZCA	20	-36.67434	-97.06581	24.94	91.21	87.53	150.50	635.48	3.91	1542099
NZ-AN	NAZCA	21	-35.74185	-104.09239	24.85	97.45	16.33	635.48	57.48	3.65	757176
NZ-AN	NAZCA	22	-35.52024	-104.68559	24.82	97.98	16.85	57.48	419.22	3.80	509903
NZ-AN	NAZCA	23	-34.57586	-109.24777	24.77	102.04	29.88	419.22	0.00	2.14	831177

Nazca – $Vol_{<150℃}$ = 6.657 10^6 m^3/yr – Mg_{rel} = 0.275 10^{11} mol/yr

Vol_{MORB} = 1020.456·10^6 m^3/yr

South East Indian Ridge (SEIR)

Plate	*Ridge*	*#*	*Lat*	*Long*	V_s	α_s	L_{seg}	L_{off}^1	L_{off}^2	H_c	$Vol_{<150℃}$
CP-AN	SEIR	1	-25,84694	70,27286	26,83	46,18	82,89	0,00	23,24	8,10	0
CP-AN	SEIR	2	-26,13218	70,81129	27,00	45,85	34,78	23,24	42,60	7,56	0
CP-AN	SEIR	3	-26,16140	71,41515	27,12	45,35	54,03	42,60	10,33	7,92	0
CP-AN	SEIR	4	-26,85161	72,25254	27,43	44,96	177,81	10,33	25,30	7,90	0
CP-AN	SEIR	5	-27,42965	73,20802	27,72	44,42	30,14	25,30	25,51	8,08	0

CP-AN	SEIR	6	-27,79344	73,96345	27,93	43,96	130,87	25,51	39,55	7,75	0
CP-AN	SEIR	7	-29,08554	74,81921	28,33	43,80	183,45	39,55	33,82	7,72	0
CP-AN	SEIR	8	-30,31043	75,68613	28,69	43,58	130,92	33,82	21,83	7,88	0
CP-AN	SEIR	9	-31,18337	76,34723	28,95	43,38	96,70	21,83	27,56	7,97	0
CP-AN	SEIR	10	-32,36443	77,17407	29,27	43,15	198,60	27,56	34,75	7,87	0
CP-AN	SEIR	11	-33,33841	77,65841	29,50	43,10	25,11	34,75	47,62	7,47	0
CP-AN	SEIR	12	-34,44521	78,07937	29,72	43,13	208,97	47,62	56,42	7,92	0
CP-AN	SEIR	13	-35,94481	78,74977	30,03	43,06	115,34	56,42	132,27	7,38	0
CP-AN	SEIR	14	-37,43572	78,35625	30,19	43,82	69,08	132,27	51,81	6,98	0
CP-AN	SEIR	15	-38,16317	78,40363	30,30	43,99	48,56	51,81	223,88	5,96	132172
CP-AN	SEIR	16	-40,07136	77,25026	30,44	45,48	61,46	223,88	0,00	6,46	129339
AU-AN	SEIR	1	-40,81850	78,43699	31,14	49,24	270,07	0,00	110,57	8,17	0
AU-AN	SEIR	2	-41,99447	82,21172	31,90	46,12	303,04	110,57	293,42	7,64	544159
AU-AN	SEIR	3	-41,54568	87,04659	32,47	41,62	232,10	293,42	60,96	7,51	528846
AU-AN	SEIR	4	-42,51515	90,06473	33,00	39,32	294,20	60,96	30,35	7,98	0
AU-AN	SEIR	5	-44,24774	94,06883	33,66	36,44	455,42	30,35	76,60	8,00	0
AU-AN	SEIR	6	-46,14321	96,06733	34,05	35,25	52,50	76,60	38,15	7,54	0
AU-AN	SEIR	7	-47,39886	97,73165	34,30	34,15	312,12	38,15	135,55	7,98	0
AU-AN	SEIR	8	-47,81825	102,37492	34,65	30,40	326,28	135,55	52,37	8,03	0
AU-AN	SEIR	9	-48,12577	105,08713	34,83	28,25	99,41	52,37	81,87	7,66	0
AU-AN	SEIR	10	-49,17518	105,67695	34,90	27,93	82,11	81,87	136,25	7,17	0
AU-AN	SEIR	11	-48,53689	107,78575	34,97	26,15	127,79	136,25	23,96	7,65	0
AU-AN	SEIR	12	-49,08807	108,63942	35,02	25,53	35,95	23,96	21,36	8,04	0
AU-AN	SEIR	13	-49,58407	109,64260	35,07	24,78	170,83	21,36	26,99	8,10	0
AU-AN	SEIR	14	-49,78219	111,11244	35,12	23,62	39,62	26,99	19,91	8,09	0
AU-AN	SEIR	15	-50,18597	111,95031	35,15	22,98	107,35	19,91	26,05	8,13	0
AU-AN	SEIR	16	-50,25773	113,36744	35,18	21,86	83,78	26,05	65,56	7,78	0
AU-AN	SEIR	17	-49,95487	114,92113	35,20	20,61	83,09	65,56	16,84	7,98	0
AU-AN	SEIR	18	-49,94726	115,72540	35,20	19,97	19,28	16,84	92,05	7,51	0
AU-AN	SEIR	19	-49,30356	116,74738	35,20	19,15	41,86	92,05	13,13	7,49	0
AU-AN	SEIR	20	-49,52632	117,21421	35,21	18,79	36,23	13,13	15,91	8,75	0
AU-AN	SEIR	21	-49,82932	117,92940	35,21	18,24	82,62	15,91	18,44	8,38	0
AU-AN	SEIR	22	-49,96419	119,34933	35,21	17,13	117,11	18,44	99,48	7,88	0
AU-AN	SEIR	23	-49,30239	120,62332	35,20	16,15	18,21	99,48	56,09	7,08	0
AU-AN	SEIR	24	-48,92161	121,30671	35,19	15,63	49,63	56,09	79,19	7,18	0
AU-AN	SEIR	25	-49,79300	121,92362	35,18	15,13	92,43	79,19	50,44	7,74	0
AU-AN	SEIR	26	-49,53090	123,03901	35,16	14,28	32,39	50,44	62,02	7,44	0
AU-AN	SEIR	27	-49,05103	123,65987	35,15	13,83	25,05	62,02	30,55	7,56	0
AU-AN	SEIR	28	-48,97283	124,57154	35,12	13,14	99,19	30,55	55,00	7,87	0
AU-AN	SEIR	29	-49,70757	125,49096	35,09	12,38	59,57	55,00	128,61	6,95	0
AU-AN	SEIR	30	-48,75649	126,86165	35,05	11,41	91,15	128,61	122,78	7,00	0
AU-AN	SEIR	31	-50,21025	129,01963	34,95	9,61	277,22	122,78	11,54	8,17	0
AU-AN	SEIR	32	-50,61282	131,16987	34,84	7,89	37,19	11,54	49,68	8,03	0
AU-AN	SEIR	33	-50,32167	133,33936	34,71	6,25	253,36	49,68	32,47	7,96	0
AU-AN	SEIR	34	-50,21270	137,47217	34,40	3,06	326,99	32,47	172,12	7,89	0
AU-AN	SEIR	35	-51,83713	140,11733	34,17	0,57	58,17	172,12	230,45	5,45	100854
AU-AN	SEIR	36	-53,93085	140,73542	34,13	359,53	36,01	230,45	23,52	6,36	67482
AU-AN	SEIR	37	-54,18827	142,56802	33,96	357,93	203,51	23,52	65,14	8,01	0
AU-AN	SEIR	38	-54,78341	145,54802	33,67	355,23	183,67	65,14	315,54	7,22	586135
AU-AN	SEIR	39	-57,50392	148,16284	33,47	352,04	14,26	315,54	67,90	4,85	525661
AU-AN	SEIR	40	-58,05547	148,69879	33,43	351,37	16,08	67,90	180,97	6,14	0
AU-AN	SEIR	41	-59,55336	150,02944	33,35	349,63	38,72	180,97	103,35	5,73	0

AU-AN	SEIR	42	-60,14462	152,19274	33,16	347,41	162,87	103,35	358,50	6,92	728530
AU-AN	SEIR	43	-62,14109	158,68057	32,63	340,42	287,37	358,50	82,24	7,55	750952
AU-AN	SEIR	44	-61,91622	162,39587	32,21	336,88	58,24	82,24	0,00	7,86	0
PA-AN	SEIR	1	-61,91622	162,39587	21,97	324,89	58,24	0,00	85,98	6,90	0
PA-AN	SEIR	2	-62,20906	164,34632	22,42	324,61	64,62	85,98	100,69	5,63	0
PA-AN	SEIR	3	-62,59358	166,51277	22,87	324,35	65,26	100,69	10,81	6,56	0
PA-AN	SEIR	4	-62,43952	167,30994	23,16	323,78	18,96	10,81	118,75	6,30	0
PA-AN	SEIR	5	-62,98177	169,59011	23,56	323,63	77,85	118,75	128,15	5,49	0
PA-AN	SEIR	6	-63,46578	172,50893	24,14	323,04	84,21	128,15	150,12	5,65	27992
PA-AN	SEIR	7	-64,24544	175,33684	24,54	322,81	28,54	150,12	61,30	5,34	3502
PA-AN	SEIR	8	-64,53652	176,53038	24,72	322,63	23,06	61,30	37,12	6,68	0
PA-AN	SEIR	9	-64,67285	177,38597	24,87	322,39	21,72	37,12	77,74	6,25	0
PA-AN	SEIR	10	-65,07613	178,87740	25,07	322,19	34,69	77,74	87,35	5,83	0
PA-AN	SEIR	11	-65,35813	-178,99829	25,46	321,47	69,27	87,35	0,00	7,23	0

SEIR – $Vol_{<150℃}$ = 4.125 10^6 m^3/yr – Mg_{rel} = 0.170 10^{11} mol/yr

Vol_{MORB} = 3938.797·10^6 m^3/yr

Galapagos Ridge

Plate	*Ridge*	*#*	*Lat*	*Long*	V_s	α_s	L_{seg}	L_{off}^1	L_{off}^2	H_c	$Vol_{<150℃}$
CO-NZ	Galap	1	4,43769	-82,42040	30,77	359,37	22,60	0,00	81,05	8,06	0
CO-NZ	Galap	2	3,73354	-82,74569	30,67	359,74	27,63	81,05	56,77	6,65	0
CO-NZ	Galap	3	3,29581	-83,59234	30,41	359,94	146,05	56,77	129,93	7,64	0
CO-NZ	Galap	4	2,20103	-84,53967	30,12	0,55	21,08	129,93	62,85	6,14	0
CO-NZ	Galap	5	1,66408	-84,95896	29,99	0,86	53,55	62,85	110,37	6,73	0
CO-NZ	Galap	6	0,80288	-86,19891	29,59	1,40	184,55	110,37	26,51	7,78	0
CO-NZ	Galap	7	0,81165	-88,88231	28,67	1,40	395,24	26,51	109,81	7,86	0
CO-NZ	Galap	8	2,26923	-93,17518	27,05	0,20	515,66	109,81	43,24	7,74	0
CO-NZ	Galap	9	2,29465	-95,99881	25,91	0,07	103,88	43,24	33,27	7,36	0
CO-NZ	Galap	10	2,24114	-97,71510	25,19	0,05	257,02	33,27	26,87	7,44	0
CO-NZ	Galap	11	2,28475	-99,37842	24,47	359,94	106,42	26,87	20,49	7,52	0
CO-NZ	Galap	12	2,23886	-100,08894	24,16	359,96	46,55	20,49	0,00	7,99	0

Galapagos – $Vol_{<150℃}$ = 0.0 m^3/yr – Mg_{rel} = 0.0 mol/yr

Vol_{MORB} = 791.925·10^6 m^3/yr

Table S2. *Bulk rock composition of samples from the Vema Lithospheric Section*[25]*. Data show a variety of serpentinized rocks, texturally ranging from porphyroclastic to mylonitic.*

Sample	SiO2	TiO2	Al2O3	FeOtot	MnO	MgO	CaO	Na2O	K2O	P2O5	LOI	Sum
S19-02/21	39.61	0.07	1.23	7.5866	0.1	35.83	1.38	0.38	0.02	0.04	13.1	99.32
S19-02/22	40.06	0.06	2.82	8.3215	0.12	33.49	2.17	0.66	0.03	0.06	11.5	99.25
S19-02/26	37.8	0.06	0.82	10.247	0.12	35.39	0.58	0.68	0.03	0.09	13.2	99.03
S19-03/25	40.40	0.06	1.19	6.95	0.08	37.08	0.95	0.39	0.03	0.04	12.2	99.40
S19-04/64	39.6	0.03	1.31	7.6315	0.25	37.22	0.48	0.28	0.04	0.06	12.4	99.25
S19-07/23	40.42	0.12	2.68	7.04	0.19	35.87	1.36	0.30	0.04	0.05	11.3	99.39
S19-07/30	39.34	0.01	0.91	8.47	0.12	36.29	0.61	0.47	0.04	0.05	12.9	99.21
S19-12/04	39.73	0.07	2.44	12.04	0.22	32.26	3.57	0.54	0.04	0.15	7.8	98.86
S19-12/33	36.64	0.08	2.49	15.86	0.40	30.75	2.85	0.81	0.07	0.24	8.2	98.43
S19-13/36	37.13	0.04	1.20	8.18	0.10	35.42	3.51	0.37	0.02	0.05	13.2	99.23
S19-13/37	44.92	0.04	1.00	10.19	0.14	30.29	2.49	0.66	0.10	0.05	9.2	99.08
S19-15/17	39.67	0.04	2.07	9.78	0.18	33.79	1.32	0.51	0.06	0.11	11.5	99.05
S19-15/70	38.90	0.04	1.67	10.98	0.17	34.42	1.65	0.51	0.04	0.13	10.4	98.93
S19-20/85	37.98	0.10	3.00	12.18	0.35	30.54	3.02	0.55	0.05	0.15	10.9	98.79
S19-05/55	40.59	0.01	1.14	8.14	0.16	36.51	0.47	0.34	0.03	0.03	11.9	99.28
S19-05/64	41.19	0.02	1.25	6.26	0.12	38.35	0.43	0.25	0.02	0.01	11.6	99.52
S19-05/84	40.69	0.02	0.68	8.50	0.15	37.04	0.67	0.35	0.03	0.04	11.1	99.25
S19-23/39	40.48	0.02	1.36	5.95	0.09	38.81	0.16	0.21	0.02	0.02	12.4	99.54
S19-23/41	39.97	0.02	1.16	6.22	0.10	38.98	0.21	0.19	0.01	0.02	12.6	99.50
S19-23/45	40.01	0.02	1.24	8.09	0.11	37.56	0.78	0.32	0.03	0.06	11.1	99.33
S19-23/46	40.20	0.03	1.59	7.88	0.16	37.38	0.66	0.41	0.06	0.05	10.9	99.35
S19-23/49	40.51	0.03	1.22	6.93	0.11	38.05	0.23	0.45	0.05	0.03	11.8	99.41
S19-24/19	40.17	0.04	1.32	8.29	0.15	36.05	1.46	0.34	0.02	0.05	11.4	99.25
S19-25/71	40.49	0.01	0.52	8.18	0.08	36.57	0.85	0.32	0.03	0.03	12.2	99.27
S19-27/01	40.23	0.03	1.58	6.41	0.18	38.49	0.62	0.26	0.04	0.03	11.6	99.46
S19-28/23	40.32	0.02	1.39	7.39	0.24	37.04	0.97	0.29	0.03	0.04	11.6	99.31
S19-30/30	39.10	0.01	0.71	7.30	0.20	39.30	0.06	0.23	0.02	0.03	12.3	99.29
S19-30/72	39.59	0.04	1.39	6.25	0.36	38.77	0.30	0.27	0.03	0.03	12.5	99.50
S19-30/79	40.80	0.02	1.76	10.03	0.16	33.22	1.65	0.30	0.03	0.11	11.2	99.29

Table S3. *Reconstructed primary bulk rock major elements of samples from the Vema Lithospheric Section*[26].

		reconstr. bulk rock			rock mode weight				rock mode volume				estimated olivine			opx			cpx			sp		
sample	sum	Sitot	Mgtot	Fetot	ol	opx	cpx	sp	ol	opx	cpx	sp	Mgol	Feol	Si	SiO2	FeO	MgO	SiO2	FeO	MgO	SiO2	FeO	MgO
S1902-05	97.80	43.48	45.83	8.49	0.780	0.190	0.023	0.009	0.778	0.190	0.023	0.009	50.04	9.18	40.78	55.14	6.05	33.11	51.45	2.58	16.46	0.02	13.45	17.50
S1902-07	96.48	44.66	43.71	8.11	0.678	0.280	0.032	0.013	0.675	0.279	0.032	0.013	49.96	9.20	40.85	54.74	5.84	32.71	51.49	2.17	15.73	0.02	13.27	17.32
S1904-38A	95.98	43.44	44.04	8.50	0.711	0.251	0.015	0.021	0.709	0.251	0.015	0.021	49.81	9.37	40.83	54.30	6.07	32.25	51.13	2.45	16.32	0.04	13.03	17.40
S1904-39	97.65	45.63	43.86	8.16	0.653	0.317	0.032	0.005	0.647	0.315	0.032	0.005	50.02	9.28	40.70	54.90	6.18	33.44	51.10	2.39	16.14	0.02	13.45	18.10
S1904-40A	97.08	43.36	45.34	8.38	0.758	0.215	0.011	0.016	0.756	0.215	0.011	0.016	50.02	9.12	40.86	55.07	5.77	32.79	51.62	2.06	16.29	0.00	13.31	17.07
S1904-42A	95.17	44.20	42.71	8.26	0.646	0.296	0.037	0.021	0.645	0.296	0.037	0.021	49.81	9.42	40.77	53.98	6.12	32.64	51.06	2.36	15.96	0.01	12.92	17.27
S1905-59	93.04	45.91	39.47	7.66	0.535	0.333	0.112	0.022	0.532	0.332	0.112	0.022	49.86	9.30	40.84	54.96	6.30	32.10	51.39	2.43	15.97	0.01	14.30	16.76
S1912-04A	90.55	44.29	38.67	7.59	0.536	0.286	0.131	0.041	0.537	0.288	0.132	0.041	49.93	9.25	40.81	54.90	6.10	32.57	51.34	2.85	15.95	0.00	12.70	18.71
S1912-06	95.45	44.02	43.10	8.33	0.687	0.249	0.046	0.018	0.684	0.249	0.046	0.018	49.79	9.37	40.84	54.63	6.20	31.92	50.97	2.76	15.37	0.01	12.32	18.78
S1913-01	94.90	43.19	43.42	8.29	0.716	0.203	0.055	0.023	0.716	0.204	0.055	0.023	49.88	9.28	40.84	54.70	6.04	32.32	51.30	2.56	15.57	0.01	11.94	18.87
S1913-07A	92.72	43.89	40.70	8.13	0.599	0.294	0.070	0.033	0.600	0.295	0.070	0.033	49.71	9.46	40.83	54.06	6.18	31.85	50.85	3.17	16.16	0.00	12.90	18.97
S1923-38A	96.95	43.20	45.06	8.69	0.748	0.233	0.000	0.018	0.747	0.233		0.018	49.84	9.38	40.78	54.55	6.24	32.41	50.98	2.37	15.98	0.00	12.56	18.07
S1923-42A	96.51	42.42	45.48	8.61	0.779	0.190	0.002	0.024	0.781	0.191	0.002	0.024	49.98	9.19	40.83	55.23	6.03	32.58	51.36	2.37	16.03	0.02	12.67	18.10
S1923-84A	96.79	42.97	45.26	8.57	0.764	0.195	0.023	0.017	0.763	0.195	0.023	0.017	49.99	9.29	40.72	54.83	6.12	33.22	50.95	2.67	16.44	0.02	12.50	18.39
S1923-86A	94.95	41.90	44.25	8.80	0.739	0.204	0.012	0.036	0.745	0.206	0.012	0.036	49.90	9.39	40.71	54.88	6.50	32.71	50.93	2.59	16.12	0.01	14.06	17.41
S1924-01A	95.23	42.73	44.20	8.31	0.758	0.146	0.074	0.020	0.758	0.146	0.074	0.020	50.05	9.21	40.74	55.22	6.18	33.27	51.38	2.45	15.56	0.02	12.55	18.84
S1924-04	96.17	45.34	42.59	8.25	0.632	0.321	0.036	0.014	0.628	0.320	0.036	0.014	49.86	9.31	40.83	54.99	6.43	32.12	51.58	3.50	15.85	0.00	12.09	19.30
S1924-12	93.02	40.99	43.22	8.81	0.744	0.155	0.045	0.042	0.752	0.157	0.046	0.043	49.71	9.58	40.71	54.08	6.60	32.25	50.55	2.48	14.80	0.00	12.70	19.17
S1927-03A	96.20	43.43	44.25	8.52	0.736	0.200	0.048	0.016	0.734	0.200	0.048	0.016	49.91	9.36	40.73	55.01	6.43	32.61	50.90	2.88	16.36	0.00	13.00	17.83
S1927-05A	95.72	43.35	43.84	8.54	0.707	0.238	0.031	0.022	0.706	0.238	0.031	0.022	49.86	9.40	40.74	54.42	6.41	32.75	51.36	2.57	16.21	0.01	12.95	17.94
S1928-09A	93.26	45.18	40.19	7.89	0.545	0.360	0.065	0.029	0.543	0.360	0.065	0.029	49.84	9.37	40.78	54.60	6.21	32.36	50.89	2.69	15.54	0.03	13.00	18.16
S1928-10	94.33	43.90	42.23	8.20	0.627	0.310	0.028	0.031	0.633	0.314	0.028	0.031	49.88	9.34	40.78	54.51	5.99	32.58	50.74	2.71	15.35	0.03	13.06	17.92
S1928-15A	93.93	44.06	41.70	8.17	0.619	0.296	0.052	0.030	0.618	0.297	0.052	0.030	49.88	9.35	40.77	54.69	6.20	32.52	50.92	2.66	15.58	0.02	13.79	17.83
S1928-19	94.67	43.37	42.97	8.34	0.677	0.253	0.037	0.029	0.679	0.254	0.037	0.029	49.91	9.32	40.78	54.92	6.17	32.51	50.86	2.63	15.75	0.03	12.94	18.09
S2209-01A	97.50	43.40	45.48	8.62	0.787	0.163	0.048	0.005	0.784	0.163	0.048	0.005	49.85	9.41	40.74	54.35	6.15	32.72	50.72	2.76	16.81	0.02	15.13	16.29
S2220-04	98.16	43.98	45.72	8.47	0.761	0.228	0.006	0.008	0.758	0.228	0.006	0.008	50.00	9.17	40.83	55.19	5.98	32.71	51.46	2.76	16.41	0.01	13.83	17.30
S2220-06	98.76	43.68	46.45	8.63	0.802	0.187	0.013	0.003	0.798	0.186	0.013	0.003	50.00	9.22	40.78	55.30	6.13	32.72	51.09	3.01	16.45	0.04	16.08	16.57
S2221-01A	95.16	45.15	42.01	7.99	0.608	0.315	0.064	0.016	0.606	0.315	0.064	0.016	49.92	9.39	40.69	54.51	6.12	33.09	50.45	2.45	15.99	0.02	12.41	18.00
S2221-04B	96.61	43.04	44.87	8.70	0.755	0.199	0.030	0.016	0.755	0.199	0.030	0.016	49.85	9.45	40.70	54.29	6.38	32.90	50.87	2.85	16.13	0.01	13.46	17.68
S2221-05B	97.13	43.52	45.04	8.57	0.752	0.215	0.023	0.012	0.750	0.215	0.023	0.012	49.88	9.37	40.75	54.54	6.12	32.72	50.75	2.78	15.66	0.00	12.91	17.67
P7003-23A	98.16	42.20	47.25	8.71	0.857	0.120	0.011	0.011	0.858	0.120	0.011	0.011	50.07	9.10	40.83	55.26	6.02	33.12	52.10	2.67	17.13	0.00	14.66	16.27

Table S4. *Regression results and correlation values. Regressions have been performed for each oxide pair in order to derive the correlation between major oxides in pyroxenes and in olivine. Plots refer to panels in figure S7.*

		Mg_{Ol}			Si_{Ol}			Fe_{Ol}		
		Int	**Slope**	**R^2**	**Int**	**Slope**	**R^2**	**Int**	**Slope**	**R^2**
Plot 1- $\mathbf{Mg_{opx}}$	Value	34.20	0.479	0.46	38.30	0.074	0.02	21.09	-0.372	0.36
	σ	1.40	0.043		1.33	0.041		1.33	0.041	
Plot 2- $\mathbf{Si_{opx}}$	Value	28.90	0.378	0.43	33.14	0.138	0.11	29.35	-0.369	0.54
	σ	1.96	0.036		1.73	0.032		1.55	0.028	
Plot 3- $\mathbf{Fe_{opx}}$	Value	52.78	-0.547	0.11	42.35	-0.289	0.06	3.96	0.893	0.41
	σ	0.72	0.124		0.52	0.090		0.51	0.089	
Plot 4- $\mathbf{Mg_{cpx}}$	Value	49.82	-0.010	0.01	39.94	0.041	0.01	9.85	-0.041	0.01
	σ	0.59	0.034		0.40	0.023		0.49	0.028	
Plot 5- $\mathbf{Si_{cpx}}$	Value	35.66	0.271	0.24	34.15	0.126	0.11	24.79	-0.304	0.45
	σ	2.00	0.039		1.49	0.029		1.40	0.027	
Plot 6- $\mathbf{Fe_{cpx}}$	Value	51.23	-0.556	0.26	40.86	-0.069	0.00	7.71	0.497	0.31
	σ	0.22	0.075		0.17	0.060		0.17	0.060	

Table S5. *Temporal variations of spreading rate (V_s), ridge length (excluding transform faults), mean crustal thickness (H_c), oceanic crustal production rate, and volume (m^3/yr) of mantle rocks ($Vol_{<150°C}$) that can interact yearly with seawater at T<150 °C estimated along present day and paleo mid-ocean ridges since 150 Ma.*

Chron	Age	Mean V_s (mm/yr)	Ridge Length (km)	Mean Hc (km)	MORB Prod. Rate (km^3/yr)	MORP T<150℃ (km^3/yr)
C1y	0.0	25.89	55875	5.58	20.35	0.2777
C5o	10.9	26.38	54460	5.93	21.66	0.2421
C6o	20.1	28.90	55122	6.13	22.43	0.2207
C13y	33.1	29.35	51638	6.21	20.87	0.2591
C18o	40.1	27.53	56008	6.02	21.82	0.2355
C21y	47.9	28.87	54624	6.08	22.01	0.2308
C25y	55.9	29.42	52276	6.23	20.94	0.2795
C31y	67.7	30.76	56142	6.64	25.82	0.1287
C34y	83.5	33.35	58855	6.89	27.31	0.0705
M0	120.4	38.13	52103	7.00	28.94	0.0431
M10	131.9	44.32	44468	7.08	28.28	0.0567
M16	139.6	43.20	48663	7.04	29.81	0.0199
M21	147.7	41.86	47120	7.01	27.32	0.0852
M25	154.3	45.88	46934	7.09	30.52	0.0068